Temporal variation in counterclockwise vertical-axis block rotations across a rift overlap zone, southwestern Ethiopia, East Africa

A. Erbello[1,2], G. Dupont-Nivet[3,5], T. Kidane[4], N. Nowaczyk[5], M. Sudo[1], D. Melnick[6], B. Bookhagen[1], S. Brune[5,1], G. Corti[7], G. Gecho[8], and M.R. Strecker[1]

[1]Institute of Geosciences, University of Potsdam, Potsdam, Germany.

[2]Now at Applied Geology Department, School of Natural Sciences, Adama Science and Technology University, Adama, Ethiopia.

[3]Géosciences Rennes, UMR 6118, Université de Rennes 1, Rennes, France.

[4]Environmental Science and Geology Department, College of Liberal Arts and Sciences, Wayne State University, USA.

[5]Helmholtz Centre Potsdam-GFZ German Research Centre for Geosciences, Potsdam, Germany.

[6]Instituto de Ciencias de la Tierra, Universidad Austral de Chile, Valdivia, Chile

[7]Consiglio Nazionale delle Ricerche, Istituto di Geoscienze e Georisorse, Firenze, Italy.

[8]Arba-Minch University, College of Natural and Computational Sciences, Geology Department, Arba-Minch, Ethiopia.

Corresponding author: Asfaw Erbello (asfaw.erbello@astu.edu.et, asfaw.erbello.doelesso@uni-potsdam.de)

Highlights:

- Paleomagnetic results from the extensional overlap zone of the Gidole plateau between the southern Main Ethiopian Rift and the Chew Bahir-Gofa Province reveal counterclockwise vertical-axis rotations.
- The extent of the vertical-axis block rotations progressively decreased from Oligocene to Miocene following the regional patterns of deformation.
- The deformation associated with the vertical-axis block rotations was likely associated with the reactivation of inherited NW-SE-striking basement fabrics.

Abstract

The southward propagation of the southern Main Ethiopian Rift (sMER) and the northward propagation of the Kenya Rift have generated the Broadly Rifted Zone (BRZ), a ~40-km-wide region of extensional overlap between the Chew Bahir Basin-Gofa Province and the sMER. However, the tectonic interaction between these propagating rifts is not well-understood. We present new paleomagnetic and geochronologic data from Eo–Oligocene (45–35 Ma) and Miocene (18–11 Ma) volcanic and sedimentary rocks from the BRZ. Rock magnetic, alternating field and thermal demagnetization experiments indicate simple titanomagnetite mineralogies carrying a characteristic remanent magnetization from which straightforward magnetization directions were obtained. Site-mean paleomagnetic directions obtained from the analyzed samples reflect stable normal and reversed polarity directions. A comparison of the mean directions obtained for the Eo–Oligocene and Miocene rocks relative to the pole for stable South Africa at the corresponding ages reveals a significant counterclockwise (CCW) rotation of ~11.1° ± 6.4° and insignificant CCW rotation of ~3.2° ± 11.5°, respectively, reflecting a decrease in the extent of block rotations through time. Our results are consistent with the regional migration patterns of deformation during rifting. In the context of the regional tectonic evolution toward a narrow zone of extension, much of the deformation associated with block rotations probably occurred prior to the final stages of the emplacement of the Miocene volcanic flows. In light of the structural fabrics in the basement rocks exposed in the sMER, the observed CCW block rotations were likely accompanied and aided by the reactivation of NW-SE-striking basement heterogeneities, supporting the notion that inherited crustal-scale structures play a significant role during rifting across the BRZ.

1 Introduction

Continental rifts are nascent extensional plate boundaries and commonly evolve from the growth of normal-fault bounded, initially isolated basins to linked graben systems, and ultimately ocean basins (e.g., Ebinger et al., 1999; Ebinger and Scholz, 2012 and references therein). In map view, these fault-bounded basins are often laterally separated from each other. A lateral transfer of extensional strain between these basins is thus required over time to kinematically link these different sites of tectonic subsidence and extension and to maintain crustal extension between spatially disparate rift segments (e.g., Rosendahl, 1987; Childs et al., 1993, 1995). The structural character of rift-transfer zones may be further complicated either when the transfer of strain is associated with the reactivation of inherited crustal-scale heterogeneities or if rotations are involved to accommodate the differential motion of crustal blocks (e.g., Bosworth 1985; Rosendahl et al., 1987; Morley et al., 1990, 1992; Dawers and Anders, 1995; Peacock, 2002; Hetzel and Strecker, 1994; Bosworth, 1992; Corti, 2008;). The topographic relief patterns of such transfer zones may exert a crucial influence not only on the dispersal patterns of biota and thus on biodiversity (e.g., Dommain et al., 2022), but also on the evolution of the hydrological network and sediment transport as well as on the permeability and fluid flow along individual structures (e.g., Morley et al., 1990; Nelson et al., 1992; Morley et al., 1994; Garcin et al., 2012; Dommain et al., 2022; Olaka et al., 2022).

Therefore, characterizing and understanding the kinematics of faults in transfer zones, also known as accommodation zones (e.g., Rosendahl et al., 1987), is an important step in identifying the individual stages of rift evolution and the environmental impact of fault systems, especially at the termination of rift segments and within their transfer zones. One of the tectonically active extensional regions where different types and spatial scales of rift-transfer zones can be best observed at various evolutionary stages is the Cenozoic East African Rift System (EARS). Along strike, the EARS comprises several propagating rift segments that interact via complex transfer faults, often characterized by wide zones of diffuse deformation (e.g., Rosendahl et al., 1987; Morley, 1992; Ebinger et al., 1999; Koehn et al., 2008; Brune et al., 2017; Corti et al., 2019; Kolawole et al., 2021).

With a length of ~2000 km, the EARS extends from the Afar depression in the north to Malawi and Mozambique in the south; in the Turkana depression it bifurcates into an eastern and a western branch (Fig.1a). The eastern branch, comprising the southern Afar, Main Ethiopian and Kenya rifts, is characterized by pronounced volcano-tectonic processes, whereas the western branch is volcanically less active (Fig. 1a). Geological and geophysical data from the western and eastern branches indicate that many of the adjacent rift segments are linked by transfer faults (e.g., Kolawole et al., 2021); often, fault motion within such transfer zones is influenced by inherited structures related to earlier deformation processes (e.g., Versfelt and Rosendahl, 1989; Brune et al., 2017; Corti et al., 2019). In contrast, other transfer zones in the EARS are characterized by a wide area of overlap between propagating strands of normal faults (e.g., Morley, 1994, Ebinger et al., 1999; Acocella, 2005).

Based on paleomagnetic, geodetic, seismic data, and mechanical modeling results, microplate rotations between overlapping rift segments have been inferred from different sectors in the EARS and the Afar Rift (e.g., Acton et al., 1991; Kidane et al., 2003, 2009; Koehn et al., 2008; Saria et al., 2013, 2014; Muluneh et al., 2014; Nugsse et al., 2018; Philippon et al., 2014; Brune et al., 2017; Glerum et al., 2020). While in the northern Main Ethiopian and southern Afar rifts, Kidane et al. (2003), Muluneh et al. (2014), and Nugsse et al. (2018) inferred a counterclockwise block rotation in an extensional zone located between right-stepping Quaternary magmatic segments, such paleomagnetic studies from the southern Main Ethiopian Rift, the Broadly Rifted Zone (BRZ), and farther south in the Kenya Rift and western branch of the EARS, are not available. Continuous geodetic measurements along and across the EARS indicate that the Ufipa microplate located between the left-stepping structures of the Rukwa and Tanganyika rifts (Fig. 1b) is rotating in a clockwise direction (Calais et al., 2006; Fernandes et al., 2013; Deprez et al., 2013; Saria et al., 2013, 2014; Stamps et al., 2008, 2018, 2021).

Farther north in the western branch of the EARS, numerical and analog modeling of extensional structures (e.g., Koehn et al., 2008; Ayue and Koehn; 2010) have also indicated a clockwise rotation of the Rwenzori microplate, which is located between the left-stepping structures that delimit the Edward and Albert rifts (Fig. 1c). Similarly, counterclockwise rotation involving reactivated Mesozoic crustal anisotropies affects an uplifted crustal block between right-stepping rift segments of the Chew Bahir-Gofa Province and the southern Main Ethiopian rift (e.g., Philippon et al., 2014; Brune et al., 2017; Sullivan et al., 2024). Finally, and at a much larger spatial scale, a counterclockwise rotation of a mechanically strong, undeformed layer of the Victoria microplate located between the right-stepping eastern and western branches of the EARS was inferred by Glerum et al. (2020) (Fig. 1d). These findings show that the type of rift overlap (right- or left-stepping) controls the direction of microplate rotation across all relevant scales because the geometric relationship between stepover and rotation is scale-invariant (McKenzie and Jackson, 1986; Schouten et al., 1993; Katz et al., 2005; Koehn et al., 2010; Glerum et al., 2020).

Taken together, the inferred microplate rotations between the propagating structures of the Rukwa and Tanganyika rifts (Ufipa Horst), the Edward and Albert rifts (Rwenzori microplate), the eastern and western branches of the EARS (Victoria microplate), and between the southern Main Ethiopian Rift and the Chew Bahir-Gofa Province (Gidole-Chencha Horst) are mainly based on analog and numerical modeling as well as short-term geodetic observations (e.g., Stamps et al., 2008; Saria et al., 2013, 2014; Glerum et al., 2020; Philippon et al., 2014). Despite this information, the details of the structural history of many of these transfer zones has remained ambiguous, because detailed geological or paleomagnetic data do not exist to further constrain their spatiotemporal and kinematic evolution on long timescales.

Addressing this gap in knowledge, our study combines structural, geochronological, and paleomagnetic data to investigate temporally constrained deformation mechanisms during the structural linkage of rift basins. To achieve this, we chose a ~75 to 125-km-long and

~20 to 40-km-wide zone of a right-stepping rift overlap between the southern Main Ethiopian Rift and the Chew Bahir-Gofa Province in the eastern branch of the EARS for two principal reasons. First, the geochronologic constraints are excellent, and this part of the EARS is characterized by Eocene–Miocene volcanic successions (Davidson and Rex, 1980; Davidson, 1983; WoldeGabriel et al., 1991; Ebinger et al., 1993, 2000; George, 1998; George and Rogers, 2002; Bonini et al., 2005; Rooney et al., 2010) that are well-suited for additional radiometric age determination and paleomagnetic analysis of potentially rotated crustal blocks within the transfer zone. Second, extensional processes in this region have been active since ca.15 Ma (e.g., Ebinger et al., 2000; Bonini et al., 2005; Pik et al., 2008; Philippon et al., 2014; Balestrieri et al., 2016; Boone et al., 2019; Corti et al., 2019; Knappe et al., 2020; Erbello et al., 2022, 2024), and the available regional structural and stratigraphic framework allows an assessment of long-term aspects of rift-segment interaction and linkage.

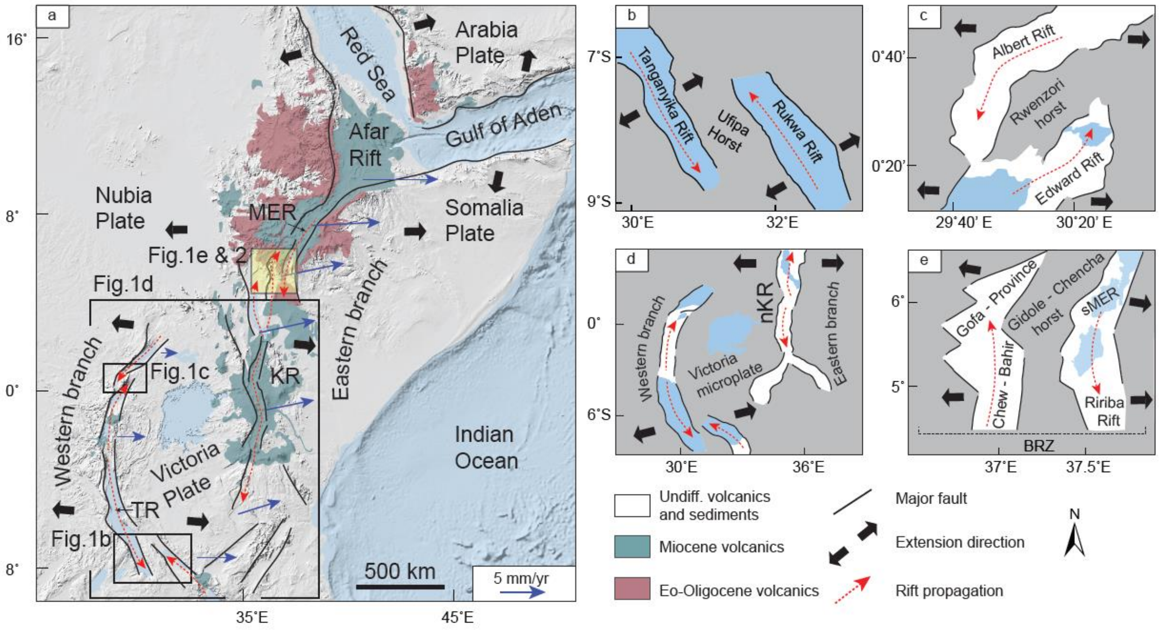

Figure 1: Tectonic setting and examples of overlapping rift segments in the East African Rift System (EARS). (a) Plate kinematics and velocity vectors (Stamps et al., 2020), principal faults, and major volcano-stratigraphic units (Rooney et al., 2017a and references therein) outcropping in the EARS (Kenya Rift, KR; Main Ethiopian Rift, MER; and Afar Rift)

superimposed on hill-shaded relief; (b–e) propagating (red arrow) and overlapping rift segments between the Tanganyika and Rukwa rifts (b); Albert and Edward rifts (c); eastern and western branches of the East African Rift System (d); and the southern Main Ethiopian Rift and the Chew Bahir-Gofa Province of the study area (yellow shaded area) across the Broadly Rifted Zone (BRZ) (e).

1.1 Tectonic setting

The right-stepping propagating rift segments of the southern Main Ethiopian Rift and northern Kenya Rift interact across a wide region in southern Ethiopia, resulting in a structurally complex extensional deformation zone with imprints of multiple tectonic events. NW-SE-striking tectonic lineaments related to Cretaceous–Paleogene paleo-rifts cut obliquely NNE-SSW-striking Neoproterozoic basement fabrics (Morley et al., 1992; Bosworth and Morley, 1994; Brune et al., 2017; Emishaw and Abdelsalam, 2019), which are sub-parallel to the N-S to NE-SW-striking Cenozoic rift structures (Corti, 2009; Kendall and Lithgow-Bertelloni, 2016). The Cretaceous–Paleogene lineaments are closely associated with the locations of the Melut and Muglade rift basins in Sudan and South Sudan, and the Anza Rift in northern Kenya (e.g., Bosworth and Morley, 1994). Satellite gravity data from the BRZ reveals prominent, E-W-striking lineaments that link the Cretaceous–Paleogene rift basins in South Sudan and northern Kenya (e.g., Emishaw et al., 2019), but the structures and deposits of the N-S to NE-SW-trending Cenozoic rift basins of the active EARS mostly obscure these relationships (e.g., Ebinger et al., 1993).

Regionally, extensional deformation related to the Nubia-Somalia plate motion appears to have originated in the northern Turkana region between 35 and 25 Ma (Boone et al., 2019; Ragon et al., 2019) and migrated toward the north in the Chew Bahir Basin (e.g., Bonini et al., 2005 and references therein) by ~20 Ma (Pik et al., 2008). A recent low-temperature thermochronology study by Erbello et al. (2024) suggests that initial diffuse faulting across the BRZ likely occurred soon after the end of massive volcanism between 27 and 20 Ma. During the middle to late Miocene (15 to 6 Ma), rifting had propagated farther north into the Gofa

Province, but stalled where the extensional faults intersected pre-existing NW-SE-oriented Mesozoic lineaments (Erbello et al., 2024). This suggests that strain was accommodated along these reactivated structures that strike at high angles with respect to the overall direction of rift propagation (e.g., Molnar et al., 2019).

In the study area, extensional deformation that formed the Gidole-Chencha Horst has been associated with 20 Ma N-S-striking dikes whose emplacement may have followed the reactivation of the NW-SE-oriented lineaments (Bonini et al., 2005). This contrasts the suggestion by Ebinger et al. (2000) that the main phase of faulting along the western margin of the Chamo Basin on the eastern side of the Gidole-Chencha Horst began later, at ~15 Ma. Following the development of the western margin of the Chamo Basin, faulting migrated toward the north and south of the southern Main Ethiopian Rift during the middle Miocene (e.g., Levitte, 1974; WoldeGabriel et al., 1991; Bonini et al., 2005; Boone et al., 2019). The southward migration of deformation terminated in the Ririba Rift during the late Pliocene (e.g., WoldeGabriel et al., 1991; Levitte, 1974; Ebinger et al., 2000; Bonini et al., 2005; Corti et al., 2019; Franceschini et al., 2020).

During the Quaternary, volcanism associated with extensional faulting migrated toward the present-day narrow axial zone of the southern Main Ethiopian Rift (e.g., Woldegabriel et al., 1990; Ebinger et al., 2000), along the strike of the Turkana Rift and the lower Omo Valley (Jicha and Brown, 2014). Currently, deformation is localized in the southern Gofa Province, the Chew Bahir Basin (e.g., Ebinger et al., 2000; Philippon et al., 2014; Erbello et al., 2022, 2024), and the Segen Basin (Levitte, 1974). The strain localization in these zones of overlap has been interpreted as reflecting ongoing tectonic interaction between the southern Main Ethiopian and the northern Kenya rifts (e.g., Ebinger et al., 2000; Philippon et al., 2014; Corti et al., 2019; Knappe et al., 2020; Erbello et al., 2022) via NW-SE-striking reactivated basement fabrics (Erbello et al., 2024).

In addition to focused volcano-tectonic activity across the BRZ, normal-faulting earthquakes recorded at shallow crustal depths in the region since 1913 have clustered along a narrow zone between the lower Omo Valley, the southern Gofa Province, and the Chew Bahir and Segen basins (Gouin, 1979; Asfaw, 1990; Ayele and Arvidsson, 1997; Foster and Jackson, 1998). The limited number of earthquakes recorded a strike-slip component (Ayele, and Arvidsson, 1997 2000; Bonini et al., 2005 and references therein; Musila et al., 2023, Sullivan et al., 2024), supporting the notion that the current tectonic interaction between the southern Main Ethiopian and the northern Kenya rifts is associated with structures striking at high angle to the trend of the rift (e.g., Erbello et al., 2024).

1.2 Geologic setting

1.2.1 Neoproterozoic basement rocks

In the study area, Neoproterozoic metamorphic basement rocks comprising NNE-SSW-striking foliations have been interpreted to control the site of Cenozoic rifting in the region (Vauchez et al., 1997). High-grade amphibolites and layered granulites (Gichile, 1992), which are characterized by NNE-SSW-striking foliations (Davidson, 1983), reflect important tectono-thermal events during the collisional pan-African orogeny between 750 Ma and 550 Ma (Asrat and Barbey, 2003). Structurally and temporally related basement fabrics have been mapped in central-northern Kenya as well (e.g., Hetzel and Strecker, 1994), suggesting a structural continuity between the two areas (Gichile, 1992), as expressed by regional structures with unknown kinematics oriented sub-parallel to the Quaternary faults (e.g., Kendall and Lithgow-Bertelloni, 2016). However, local E-W-striking foliations associated with layered granulites are also known to occur along the southwest margin of the Chamo Basin, across the Konso Plateau, and in the Segen Basin (Davidson, 1983; Gichile, 1992; Asrat and Barbey, 2003). De Wit and Chewaka (1981) considered these foliations to be related to post-Pan-African tectonic events associated with the emplacement of the Konso Pluton at 449 ± 2 Ma (Asrat and Barbey, 2003). Compositionally related plutonic rocks from the west of the Konso Plateau (Davidson, 1983) and the Segen Basin margin have provided radiometric ages between 526 ± 5 Ma and

554 ± 23 Ma (Gichile, 1992; Worku and Schandelmeier, 1996; Teklay et al., 1998; Yibas et al., 2002).

1.2.2 Paleogene sedimentary rocks

The volcanic units studied by us are underlain by a thin, yet prominent and silicified basal conglomeratic sandstone that unconformably covers the crystalline basement rocks (Davidson and Rex, 1980; Ebinger et al., 1993). This unit is exposed mainly along the flanks of the Amaro Horst (WoldeGabriel, 1991; Ebinger et al., 1993), where its thickness varies from 5 to 30 m along strike (WoldeGabriel, 1991; Ebinger et al., 1993); it is absent to the west of the BRZ (Moore and Davidson, 1978; Davidson, 1983; Philippon et al., 2014). Based on the sharpness of the conformable contact with overlying Eo–Oligocene volcanic rocks and the proximal sediment-clast composition, Davidson (1983) inferred an early Paleogene depositional age for this sandstone. However, Levitte et al. (1974) suggested, on the basis of petrographic characteristics, that the unit may correspond to the late Cretaceous Turkana grits of northern Kenya (Arambourg and Wolff, 1969).

1.2.3 Eocene–Oligocene volcanic rocks

The sampled Eo–Oligocene volcanic successions are well exposed along the margins of the southern Main Ethiopian Rift, the Gofa Province, and the northern Kenya Rift, with thicknesses ranging from several hundred meters to about one kilometer (Fig. 2) (Davidson, 1983; Ebinger et al., 1993, 2000; George, 1998). Across the BRZ in southern Ethiopia, these volcanic sequences document prolonged magmatism between 45 and 28 Ma (Davidson and Rex, 1980; Davidson, 1983; Ebinger et al., 2000; George and Rogers, 2002, Rooney, 2017; Steiner et al., 2021). The study area covers the Gidole-Chencha Horst between the Chew Bahir Basin-Gofa Province and the southern Main Ethiopian Rift, where volcanic eruptive centers distributed along the margin of the Chamo and Abaya basins reflect a NW-SE-oriented extension direction (Ebinger et al., 2000). The Eocene–Oligocene volcanic successions are characterized by the

Amaro basalts, the Arba-Minch tuffs, the Gamo basalts, and the Amaro tuffs (Ebinger et al., 2000; Rooney, 2017). The ~250-m-thick tholeiitic Amaro basalt is exposed along the Amaro Horst and overlies the ubiquitous Cretaceous conglomeratic sandstone layer; it constitutes the lower section of the exposed volcanic sequences and yielded a K-Ar whole-rock age of 44.9 ± 0.7 Ma (Ebinger et al., 1993). Compositionally similar basalt flows overlie the crystalline basement rocks along the southern Amaro Horst and yielded a K-Ar age of 42.5 ± 0.7 Ma (e.g., WoldeGabriel et al., 1991). The cataclastically deformed silicic Arba-Minch tuff unit, dated at ~37 and 39 Ma, is exposed along the southwestern margin of the Chamo Basin and is overlain by the 35–37 Ma Gamo basalts and the widespread Amaro tuff unit (e.g., Ebinger et al., 2000); this unit was analyzed by the Single-Crystal Laser Fusion (SCLF) dating technique, providing an age of 33 Ma (Ebinger et al., 1993, 2000).

1.2.4 Miocene volcanic rocks

The second main phase of magmatism in southern Ethiopia is documented by a sequence of early Miocene and Pliocene basalts (Levitte et al., 1974) and N-S-striking dike swarms (Bonini et al., 2005). The Oligocene Amaro tuff is generally overlain by the ~500-m-thick Getera-Kela basalt sampled in this study, which has an age range between 18 and 11 Ma (Davidson, 1983; Ebinger et al., 1993). Interbedded fluvio-lacustrine sediments within the Getera-Kela basalts that outcrop along the south-western margin of the Chamo Basin (Ebinger et al., 1993) have been biostratigraphyically dated between 17 and 15 Ma (WoldeGabriel et al., 1991). Phonolitic eruptive centers in the Segen, Mali-Dancha, and Bala-Kela basins were dated between 16 and 12 Ma; the strike of Quaternary faults follows these eruptive centers (Davidson and Rex, 1980; Ebinger et al., 2000). The Getera-Kela volcanics are capped by a basalt that provided a whole-rock K-Ar age of ~11 Ma (WoldeGabriel et al., 1991).

1.2.5 Pliocene and Quaternary volcanic rocks

After a period of volcano-tectonic quiescence during the late Miocene (e.g., Bonini et al., 2005), early Pliocene lava flows of the Gombe Group were emplaced adjacent to the Gidole-Chencha

Horst along the Omo-Turkana Depression (Watkins, 1986; Brown et al., 1985). Although these basaltic flows were not sampled for our paleomagnetism study, they provide key markers of deformation and rift evolution. A ~5-m-thick, ~4-m.y.-old basalt is exposed in the western Usno Basin (Ebinger et al., 2000), extending ~150 km farther north along the Omo Valley (Davidson, 1983). The coeval Mursi basalts outcrop in the northern Omo Valley (Brown and Nasha, 1976). In addition, outliers of petrographically similar thin basaltic flows are exposed along the western margin of the Chew Bahir Basin (e.g., Davidson, 1983; Haileab et al., 2004). Conventional K-Ar dating of the basaltic units within the Omo-Turkana region has revealed a protracted eruptive period between ~6 and 3 Ma (e.g., Brown, 1969, Brown et al., 1985; McDougall and Watkins, 1988; McDougall, 1985). More recently, Haileab et al. (2004) suggested that these flows were emplaced at ~4 Ma and collectively called them Gombe Group basalts (Watkins, 1983), and Erbello and Kidane (2018) further specified that these thin lava flows erupted between ~4.05 and 4.18 Ma. During the late to middle Pliocene, basaltic volcanism and faulting shifted eastward in the Ririba Rift (WoldeGabriel et al., 1991; Levitte, 1974; Ebinger et al., 2000; Bonini et al., 2005; Corti et al., 2019; Franceschini et al., 2020), before magmatism became focused in a narrow zone along the Chamo Basin (e.g., Ebinger et al., 1993) and Omo Valley (Jich and Brown, 2014) during the Quaternary.

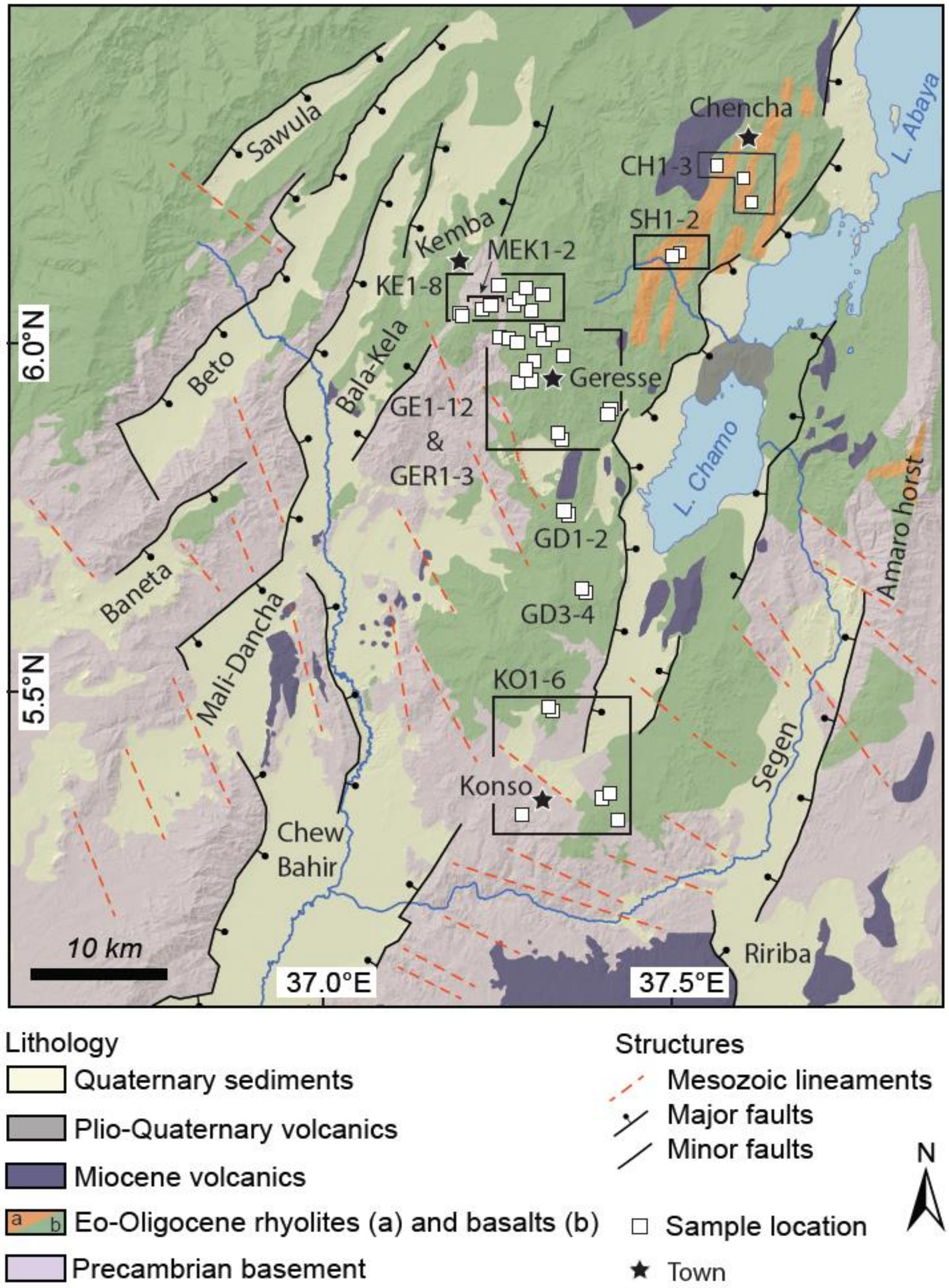

Figure 2: Geologic setting of the southern Main Ethiopian Rift and the Chew Bahir-Gofa Province (Mali-Dancha, Baneta, Beto, Bala-Kela, and Sawula basins), major stratigraphic units (Davidson, 1983; and Bonini et al., 2005), Mesozoic lineaments, and Quaternary faults

(Davidson, 1983) superimposed on hill-shaded relief. Open squares indicate sampling sites grouped by locality (black boxes).

2 Sampling and methods

Volcanic and sedimentary rocks commonly archive the Earth's magnetic field during the emplacement and/or deposition of the rock units (Cox, 1973; Tauxe and Kent, 1982; Butler, 1992; Dunlop, 1997). Subsequent tectonic movements affecting these rock units can thus be reconstructed based on the paleomagnetic directions preserved in the rocks. The well-exposed Eo–Oligocene and Miocene volcanics and sedimentary rocks from the Gidole-Chencha Horst in southern Ethiopia are ideally suited to yield paleomagnetic signals that provide information about regional tectonic deformation (Fig. 2). A total of 40 paleomagnetic sites were selected from Eo–Oligocene and Miocene volcanic (37 sites) and sedimentary rocks (3 sites), respectively (Table 1). Four to eight standard core samples were collected from each site using a gasoline-powered motor drill. Samples were oriented using a standard device with a magnetic compass and sun orientations to assess local declinations. Bedding orientations were carefully measured from the top of flows and sedimentary layers for tilt corrections. Additionally, eleven block samples (~1–1.5 kg) from representative sites were collected for ^{40}Ar/^{39}Ar dating to complement the age constraints of the sampled volcanic units (Table 2).

The paleomagnetic core samples were cut into standard specimens in sample preparation laboratories at the University of Potsdam, Germany and Addis Ababa University, Ethiopia. Natural remanent magnetization (NRM) of each specimen was measured before subjecting the specimens to incrementally increased alternative Field (AF) and thermal (TH) demagnetization experiments at the paleomagnetic laboratory of the GFZ German Research Centre for Geosciences in Potsdam. About 40 of the samples were processed thermally in the paleomagnetic laboratory of Addis Ababa University.

To define the most effective demagnetization scheme for the separation of components and determination of characteristic remanent magnetizations (ChRM) to be applied in the rest of the samples, pilot specimens (one per site) were first processed in AF, TH, and a combination of AF and TH, with detailed demagnetization steps (5 to 120 mT for AF and 20 °C to 700 °C for TH). Based on this and the rock magnetic behaviors (see 3.2.1) we ultimately applied AF demagnetizations on most of the pilot specimens resulting in a well-separated linear component with simple progressive decay. Based on these results, the bulk of the specimens was processed by 12 AF demagnetization steps (NRM, 5, 10, 15, 20, 30, 35, 40, 60, 80, 100, 120 mT). ChRM directions were obtained using a principal component analysis (Kirschvink, 1980) on a minimum of four consecutive steps following a procedure outlined in PaleoMac 6.5 (Cogné, 2003) that was also used to determine a Fisher means of the ChRM directions for each site (Fisher, 1953). To further characterize rock magnetic properties, thermomagnetic experiments were performed on representative samples using a multifunction kappabridge (MFK-1A) at GFZ Potsdam. Powdered samples of ~100 mg were incrementally heated to 700 °C and cooled back to 40 °C while bulk magnetic susceptibility was measured at a 5 °C interval.

To provide a temporal constraint of the sampled volcanic units, $^{40}Ar/^{39}Ar$ dating was performed on representative samples at the Ar/Ar Geochronology Laboratory at the University of Potsdam. The detailed Ar isotope analytical procedure is described in Wilke et al. (2010) and Halama et al. (2014). A groundmass sample (~100 mg) with grain sizes ranging between 250 and 500 μm was prepared from fresh rock collected at eleven representative sites and samples of 20 mg of each were irradiated at the Cadmium-Lined in-Core Irradiation Tube facility at the Oregon State TRIGA Reactor, USA, prior to isotopic measurement at the University of Potsdam. The mineral-age standard, the Fish Canyon Tuff sanidine FCs-EK (Morgan et al., 2014), was irradiated together with K and Ca salts. The irradiation for all samples was conducted in two phases in 2020 and 2021. The Ar isotope analyses were performed by incremental heating using a 50W continuous CO_2 laser and a Micromass 5400 noble gas mass spectrometer. Between three consecutive step-heating experiments, a blank analysis was measured for all samples. To calculate J values and unknown ages, we adopted 28.294 Ma for the FCs-EK sanidine, a decay constant for ^{40}K (Renne et al., 2011) and atmospheric Ar composition (Lee et al., 2006). The Ar isotope analysis was carried out using the "Mass Spec" software (pers. comm. A. Deino, 2020, Berkeley Geochronology Center). J values and ages were calculated using a procedure described by Uto et al. (1997). Using the age-spectrum displayed by measured apparent ages from each of the heating steps, a plateau age was determined based on a minimum of three contiguous steps with apparent age overlapping within 2σ uncertainty without the common error of the J value, and together comprising >50% of the total ^{39}Ar released (Fleck et al., 1977). In order to validate the estimated plateau ages, initial ^{40}Ar/^{36}Ar ratios obtained from normal and inverse isochrons were compared, and reflect the atmospheric value (Lee et al., 2006). Subsequently, the validated plateau ages were determined for each analyzed sample. In some cases when a plateau was not recognized, the ages were reported as an age range (probable ages) or total gas ages, following the procedure described by Schaen et al. (2020).

3 Results

3.1 ^{40}Ar/^{39}Ar-dating

From a total of eleven analyzed samples, we finally obtained six plateau ages (Fig. 3). For the remaining samples, the reported age is a total gas age or age ranges (Schaen et al., 2020). The ^{40}Ar/^{39}Ar-dating results of samples from the Gidole-Chencha Horst exhibit plateau ages ranging between 42 and 38 Ma for the Gamo-Amaro basalts and between 20 and 17 Ma for the Getera-Kela basalts. The details of the age determinations are provided in Table 1.

Sample MEK-2 collected west of the Gidole-Chencha Horst was dated at 42.441 ± 0.25 Ma, similar to a basaltic flow overlying crystalline basement in the southern Amaro Horst that was dated at 42.53 ± 0.70 Ma (WoldeGabriel et al., 1991). Similar plateau ages of 39.44 ± 0.15 Ma, 39.12 ± 0.17 Ma, and 38.31 ± 0.007 Ma were obtained at sites GD-2, GE-7, and MEK-1, respectively. However, a plateau age was not obtained for a sample at site CH-3; a total gas age estimated from the very flat age-spectrum, occupying ~70 % fraction of the total ^{39}Ar release (Fig. 3i, Table 1), records an age range between 38 and 36 Ma. Similarly, a total gas age of 35.51± 0.10 Ma was obtained for a basalt sample at site KO-4 located in the south of the Gidole-Chencha Horst. Sample GER-2 collected from the highly fractured welded tuff unit located at a higher elevation to the west of GE-7 did not yield a plateau age, but shows a relatively long flat age pattern, occupying ~80% of the total ^{39}Ar release and exhibiting an age range between 35 and 32 Ma; this provided one of the probable youngest ages of all dated Eo–Oligocene volcanic rocks (Fig. 3g). The welded tuff unit correlates with the widely distributed Amaro tuff (~33 Ma), which separates the Eo–Oligocene rock units from ~500-m-thick Miocene volcanics (Davidson, 1983; Ebinger et al., 1993; Bonini et al., 2005).

A pervasively fractured basalt flow exposed at site GE-1 yielded an Early Miocene plateau age of 19.62 ± 0.13 Ma (Fig. 3e). Farther west across the Gidole-Chencha Horst, a basalt at site GE-12, where it overlies other, sub-horizontal basalt flows (GE-10 and GE-11), was also dated, but a plateau age was not obtained. Instead, the relatively long flat age pattern, occupying ~65 % of the total ^{39}Ar release, corresponds to an age range between 21 and 19 Ma (Fig. 3h, and Table 1). These units are characterized by well-developed flow structures and no intervening paleosol horizons; possibly, these basalt sheets represent laccoliths that are closely linked with the N-S-striking dikes that were emplaced at about 20 Ma (e.g., Bonini et al., 2005). Sample KO-1 collected from a columnar-jointed basalt located to the west of the Segen basin yielded a well-constrained Miocene plateau age of 16.87 ± 0.10 Ma (Fig. 3f). Our age spectra of the Miocene volcanics are compatible with the age range of the Getera-Kela basalts between 18 and 11 Ma (Ebinger et al., 2000). Interestingly, our data suggest that regional Miocene volcanism might have started at ~20 Ma, was closely linked with diking (Bonini et al., 2005), and synchronous with faulting within the BRZ (Pik et al., 2008).

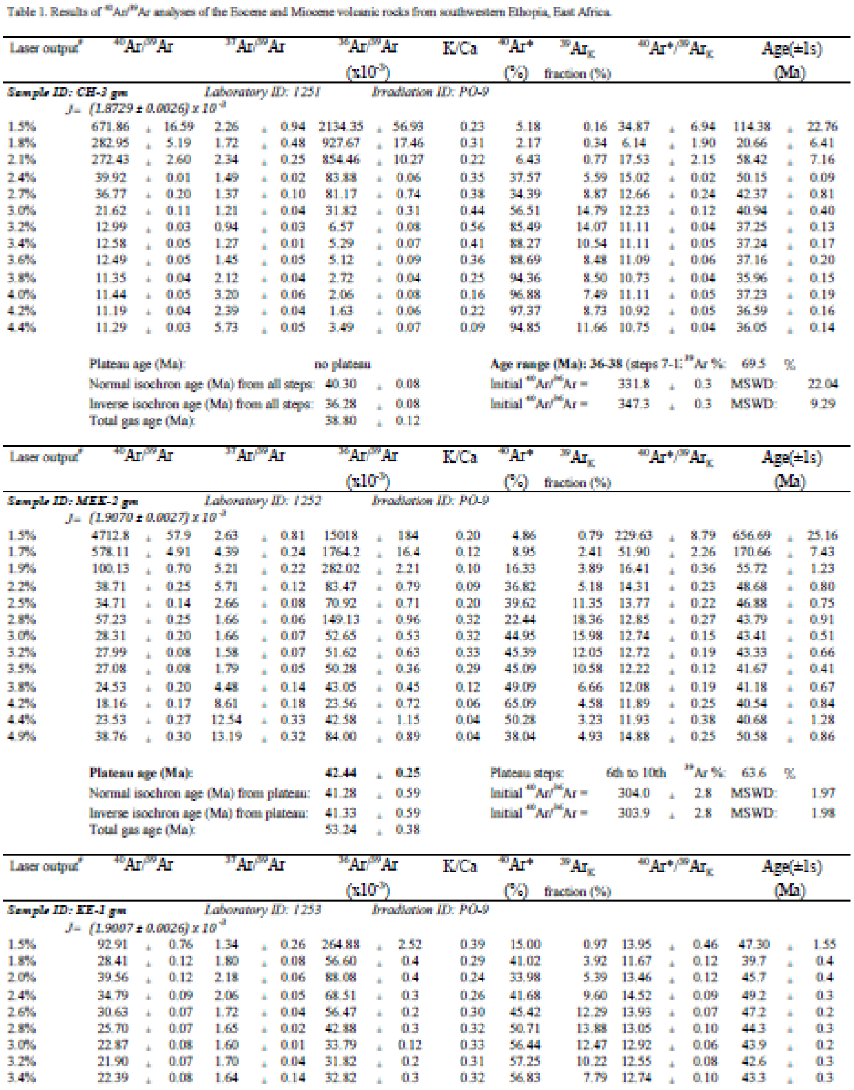

Table 1. Results of ^{40}Ar/^{39}Ar analyses of the Eocene and Miocene volcanic rocks from southwestern Ethiopia, East Africa.

Sample ID: CH-3 gm — *Laboratory ID: 1251* — *Irradiation ID: PO-9*

J= (1.8729 ± 0.0026) x 10^{-3}

Laser output^{a}	^{40}Ar/^{39}Ar	^{37}Ar/^{39}Ar	^{36}Ar/^{39}Ar (x10^{-3})	K/Ca	^{40}Ar* (%)	^{39}Ar$_K$ fraction (%)	^{40}Ar*/^{39}Ar$_K$	Age(±1s) (Ma)
1.5%	671.86 ± 16.59	2.26 ± 0.94	2134.35 ± 56.93	0.23	5.18	0.16	34.87 ± 6.94	114.38 ± 22.76
1.8%	282.95 ± 5.19	1.72 ± 0.48	927.67 ± 17.46	0.31	2.17	0.34	6.14 ± 1.90	20.66 ± 6.41
2.1%	272.43 ± 2.60	2.34 ± 0.25	854.46 ± 10.27	0.22	6.43	0.77	17.53 ± 2.15	58.42 ± 7.16
2.4%	39.92 ± 0.01	1.49 ± 0.02	83.88 ± 0.06	0.35	37.57	5.59	15.02 ± 0.02	50.15 ± 0.09
2.7%	36.77 ± 0.20	1.37 ± 0.10	81.17 ± 0.74	0.38	34.39	8.87	12.66 ± 0.24	42.37 ± 0.81
3.0%	21.62 ± 0.11	1.21 ± 0.04	31.82 ± 0.31	0.44	56.51	14.79	12.23 ± 0.12	40.94 ± 0.40
3.2%	12.99 ± 0.03	0.94 ± 0.03	6.57 ± 0.08	0.56	85.49	14.07	11.11 ± 0.04	37.25 ± 0.13
3.4%	12.58 ± 0.05	1.27 ± 0.01	5.29 ± 0.07	0.41	88.27	10.54	11.11 ± 0.05	37.24 ± 0.17
3.6%	12.49 ± 0.05	1.45 ± 0.05	5.12 ± 0.09	0.36	88.69	8.48	11.09 ± 0.06	37.16 ± 0.20
3.8%	11.35 ± 0.04	2.12 ± 0.04	2.72 ± 0.04	0.25	94.36	8.50	10.73 ± 0.04	35.96 ± 0.15
4.0%	11.44 ± 0.05	3.20 ± 0.06	2.06 ± 0.08	0.16	96.88	7.49	11.11 ± 0.05	37.23 ± 0.19
4.2%	11.19 ± 0.04	2.39 ± 0.04	1.63 ± 0.06	0.22	97.37	8.73	10.92 ± 0.05	36.59 ± 0.16
4.4%	11.29 ± 0.03	5.73 ± 0.05	3.49 ± 0.07	0.09	94.85	11.66	10.75 ± 0.04	36.05 ± 0.14

Plateau age (Ma):	no plateau		**Age range (Ma): 36-38** (steps 7-1:	^{39}Ar %:	69.5	%		
Normal isochron age (Ma) from all steps:	40.30	± 0.08	Initial ^{40}Ar/^{36}Ar =	331.8	± 0.3	MSWD:	22.04	
Inverse isochron age (Ma) from all steps:	36.28	± 0.08	Initial ^{40}Ar/^{36}Ar =	347.3	± 0.3	MSWD:	9.29	
Total gas age (Ma):	38.80	± 0.12						

Sample ID: MEK-2 gm — *Laboratory ID: 1252* — *Irradiation ID: PO-9*

J= (1.9070 ± 0.0027) x 10^{-3}

Laser output^{a}	^{40}Ar/^{39}Ar	^{37}Ar/^{39}Ar	^{36}Ar/^{39}Ar (x10^{-3})	K/Ca	^{40}Ar* (%)	^{39}Ar$_K$ fraction (%)	^{40}Ar*/^{39}Ar$_K$	Age(±1s) (Ma)
1.5%	4712.8 ± 57.9	2.63 ± 0.81	15018 ± 184	0.20	4.86	0.79	229.63 ± 8.79	656.69 ± 25.16
1.7%	578.11 ± 4.91	4.39 ± 0.24	1764.2 ± 16.4	0.12	8.95	2.41	51.90 ± 2.26	170.66 ± 7.43
1.9%	100.13 ± 0.70	5.21 ± 0.22	282.02 ± 2.21	0.10	16.33	3.89	16.41 ± 0.36	55.72 ± 1.23
2.2%	38.71 ± 0.25	5.71 ± 0.12	83.47 ± 0.79	0.09	36.82	5.18	14.31 ± 0.23	48.68 ± 0.80
2.5%	34.71 ± 0.14	2.66 ± 0.08	70.92 ± 0.71	0.20	39.62	11.35	13.77 ± 0.22	46.88 ± 0.75
2.8%	57.23 ± 0.25	1.66 ± 0.06	149.13 ± 0.96	0.32	22.44	18.36	12.85 ± 0.27	43.79 ± 0.91
3.0%	28.31 ± 0.20	1.66 ± 0.07	52.65 ± 0.53	0.32	44.95	15.98	12.74 ± 0.15	43.41 ± 0.51
3.2%	27.99 ± 0.08	1.58 ± 0.07	51.62 ± 0.63	0.33	45.39	12.05	12.72 ± 0.19	43.33 ± 0.66
3.5%	27.08 ± 0.08	1.79 ± 0.05	50.28 ± 0.36	0.29	45.09	10.58	12.22 ± 0.12	41.67 ± 0.41
3.8%	24.53 ± 0.20	4.48 ± 0.14	43.05 ± 0.45	0.12	49.09	6.66	12.08 ± 0.19	41.18 ± 0.67
4.2%	18.16 ± 0.17	8.61 ± 0.18	23.56 ± 0.72	0.06	65.09	4.58	11.89 ± 0.25	40.54 ± 0.84
4.4%	23.53 ± 0.27	12.54 ± 0.33	42.58 ± 1.15	0.04	50.28	3.23	11.93 ± 0.38	40.68 ± 1.28
4.9%	38.76 ± 0.30	13.19 ± 0.32	84.00 ± 0.89	0.04	38.04	4.93	14.88 ± 0.25	50.58 ± 0.86

Plateau age (Ma):	**42.44**	**± 0.25**	Plateau steps:	6th to 10th	^{39}Ar %:	63.6	%	
Normal isochron age (Ma) from plateau:	41.28	± 0.59	Initial ^{40}Ar/^{36}Ar =	304.0	± 2.8	MSWD:	1.97	
Inverse isochron age (Ma) from plateau:	41.33	± 0.59	Initial ^{40}Ar/^{36}Ar =	303.9	± 2.8	MSWD:	1.98	
Total gas age (Ma):	53.24	± 0.38						

Sample ID: KE-1 gm — *Laboratory ID: 1253* — *Irradiation ID: PO-9*

J= (1.9007 ± 0.0026) x 10^{-3}

Laser output^{a}	^{40}Ar/^{39}Ar	^{37}Ar/^{39}Ar	^{36}Ar/^{39}Ar (x10^{-3})	K/Ca	^{40}Ar* (%)	^{39}Ar$_K$ fraction (%)	^{40}Ar*/^{39}Ar$_K$	Age(±1s) (Ma)
1.5%	92.91 ± 0.76	1.34 ± 0.26	264.88 ± 2.52	0.39	15.00	0.97	13.95 ± 0.46	47.30 ± 1.55
1.8%	28.41 ± 0.12	1.80 ± 0.08	56.60 ± 0.4	0.29	41.02	3.92	11.67 ± 0.12	39.7 ± 0.4
2.0%	39.56 ± 0.12	2.18 ± 0.06	88.08 ± 0.4	0.24	33.98	5.39	13.46 ± 0.12	45.7 ± 0.4
2.4%	34.79 ± 0.09	2.06 ± 0.05	68.51 ± 0.3	0.26	41.68	9.60	14.52 ± 0.09	49.2 ± 0.3
2.6%	30.63 ± 0.07	1.72 ± 0.04	56.47 ± 0.2	0.30	45.42	12.29	13.93 ± 0.07	47.2 ± 0.2
2.8%	25.70 ± 0.07	1.65 ± 0.02	42.88 ± 0.3	0.32	50.71	13.88	13.05 ± 0.10	44.3 ± 0.3
3.0%	22.87 ± 0.08	1.60 ± 0.01	33.79 ± 0.12	0.33	56.44	12.47	12.92 ± 0.06	43.9 ± 0.2
3.2%	21.90 ± 0.07	1.70 ± 0.04	31.82 ± 0.2	0.31	57.25	10.22	12.55 ± 0.08	42.6 ± 0.3
3.4%	22.39 ± 0.08	1.64 ± 0.14	32.82 ± 0.3	0.32	56.83	7.79	12.74 ± 0.10	43.3 ± 0.3

3.7%	22.13	± 0.08	2.26	± 0.05	29.14	± 0.2	0.23	61.51	8.51	13.63	± 0.08	46.3	± 0.3
4.1%	24.04	± 0.10	3.22	± 0.06	39.88	± 0.3	0.16	51.56	7.58	12.42	± 0.10	42.2	± 0.3
4.4%	23.77	± 0.08	5.30	± 0.08	40.08	± 0.3	0.10	51.46	7.38	12.28	± 0.11	41.7	± 0.4

Plateau age (Ma): no plateau

Normal isochron age (Ma) from all steps: 41.93 ± 0.23 Initial ^{40}Ar/^{36}Ar = 314.7 ± 1.3 MSWD: 7.83

Inverse isochron age (Ma) from all steps: 42.00 ± 0.22 Initial ^{40}Ar/^{36}Ar = 315.7 ± 1.3 MSWD: 7.74

Total gas age (Ma): 44.47 ± 0.09

Laser output[a]	^{40}Ar/^{39}Ar		^{37}Ar/^{39}Ar		^{36}Ar/^{39}Ar (x10^{-3})		K/Ca	^{40}Ar* (%)	^{39}Ar$_K$ fraction (%)	^{40}Ar*/^{39}Ar$_K$		Age(±1s) (Ma)	
Sample ID: GER-2 gm			*Laboratory ID: 1254*			*Irradiation ID: PO-9*							
	J= (1.8887 ± 0.0026) x 10^{-3}												
1.5%	390.62	± 2.41	1.05	± 0.12	1205.7	± 8.5	0.50	7.87	2.93	30.75	± 1.36	102.07	± 4.53
1.8%	156.67	± 0.57	2.13	± 0.07	443.5	± 2.3	0.25	15.60	5.75	24.47	± 0.57	81.69	± 1.89
2.1%	39.86	± 0.19	5.89	± 0.13	83.52	± 0.79	0.09	38.62	5.09	15.45	± 0.24	52.02	± 0.80
2.4%	24.61	± 0.14	8.75	± 0.10	49.49	± 0.46	0.06	42.82	5.69	10.60	± 0.17	35.84	± 0.57
2.7%	20.40	± 0.09	5.76	± 0.10	37.04	± 0.25	0.09	48.07	9.60	9.84	± 0.08	33.30	± 0.28
2.9%	29.64	± 0.11	7.72	± 0.12	69.05	± 0.35	0.07	32.55	7.30	9.70	± 0.09	32.82	± 0.32
3.1%	21.97	± 0.09	6.29	± 0.11	42.32	± 0.26	0.08	44.81	8.64	9.89	± 0.09	33.46	± 0.30
3.3%	18.34	± 0.08	8.84	± 0.25	32.00	± 0.25	0.06	51.80	6.89	9.56	± 0.09	32.35	± 0.31
3.5%	17.22	± 0.10	9.07	± 0.14	27.43	± 0.55	0.06	56.69	6.57	9.82	± 0.18	33.23	± 0.60
3.7%	15.35	± 0.05	6.28	± 0.12	20.09	± 0.16	0.08	64.21	9.87	9.90	± 0.06	33.48	± 0.22
3.9%	18.42	± 0.06	6.28	± 0.07	30.16	± 0.22	0.08	53.87	8.68	9.96	± 0.08	33.71	± 0.26
4.1%	18.42	± 0.06	6.28	± 0.07	30.16	± 0.22	0.08	53.87	8.68	9.96	± 0.08	33.71	± 0.26
4.4%	21.58	± 0.12	6.12	± 0.12	39.93	± 0.57	0.09	47.03	6.88	10.19	± 0.17	34.47	± 0.59
4.7%	11.53	± 0.08	4.18	± 0.08	7.42	± 0.12	0.13	83.71	7.43	9.68	± 0.08	32.74	± 0.27

Plateau age (Ma): no plateau **Age range (Ma): 32-35** (steps 5-1:^{39}Ar %: 80.5 %

Normal isochron age (Ma) from all steps: 31.17 ± 0.14 Initial ^{40}Ar/^{36}Ar = 320.7 ± 0.8 MSWD: 6.53

Inverse isochron age (Ma) from all steps: 31.14 ± 0.13 Initial ^{40}Ar/^{36}Ar = 322.5 ± 0.8 MSWD: 7.00

Total gas age (Ma): 39.21 ± 0.20

Laser output[a]	^{40}Ar/^{39}Ar		^{37}Ar/^{39}Ar		^{36}Ar/^{39}Ar (x10^{-3})		K/Ca	^{40}Ar* (%)	^{39}Ar$_K$ fraction (%)	^{40}Ar*/^{39}Ar$_K$		Age(±1s) (Ma)	
Sample ID: GE-12 gm			*Laboratory ID: 1256*			*Irradiation ID: PO-9*							
	J= (1.8837 ± 0.0026) x 10^{-3}												
1.5%	1369.4	± 7.2	0.000	± 0.139	4582.1	± 25.1	7363	0.10	0.52	1.41	± 2.24	4.79	± 7.63
1.7%	558.2	± 162.7	0.015	± 0.043	1808.8	± 527.2	36	3.26	1.14	18.18	± 5.51	60.89	± 18.45
1.9%	80.66	± 0.32	0.005	± 0.009	242.5	± 1.0	112	10.24	7.12	8.26	± 0.17	27.91	± 0.57
2.1%	28.88	± 0.07	0.002	± 0.005	73.00	± 0.41	212	24.53	13.47	7.08	± 0.11	23.96	± 0.39
2.3%	18.26	± 0.05	0.001	± 0.005	38.17	± 0.68	526	37.58	11.39	6.86	± 0.20	23.22	± 0.68
2.5%	14.83	± 0.05	0.000	± 0.004	28.89	± 0.19	119807	41.84	8.46	6.20	± 0.06	21.01	± 0.19
2.7%	13.08	± 0.04	0.005	± 0.007	23.07	± 0.11	103	47.34	6.42	6.19	± 0.03	20.97	± 0.12
2.9%	11.19	± 0.05	0.000	± 0.007	16.70	± 0.12	82556	55.44	5.84	6.20	± 0.04	21.01	± 0.14
3.1%	9.58	± 0.03	0.006	± 0.008	12.09	± 0.13	91	62.34	6.24	5.97	± 0.04	20.23	± 0.15
3.3%	8.64	± 0.03	0.000	± 0.006	9.17	± 0.13	1865	68.32	6.79	5.91	± 0.04	20.00	± 0.15
3.5%	8.17	± 0.03	0.005	± 0.006	8.04	± 0.09	98	70.66	7.38	5.78	± 0.03	19.57	± 0.12
3.7%	7.91	± 0.03	0.008	± 0.006	6.82	± 0.05	65	74.25	9.07	5.87	± 0.03	19.88	± 0.10
3.9%	8.20	± 0.03	0.015	± 0.006	7.73	± 0.23	36	71.87	8.45	5.89	± 0.07	19.96	± 0.25
4.1%	9.60	± 0.05	0.013	± 0.009	12.38	± 0.11	40	61.51	4.30	5.91	± 0.04	20.00	± 0.14
4.3%	12.97	± 0.04	0.000	± 0.016	23.83	± 0.32	32241	45.14	2.31	5.85	± 0.10	19.83	± 0.33
4.5%	19.83	± 0.08	0.080	± 0.041	42.94	± 1.01	7	35.38	1.10	7.01	± 0.30	23.74	± 1.02

Plateau age (Ma): no plateau **Age range (Ma): 19-21** (steps 6-1:^{39}Ar %: 65.3 %

Normal isochron age (Ma) from all steps: 20.07 ± 0.06 Initial ^{40}Ar/^{36}Ar = 302.6 ± 0.4 MSWD: 4.99

Inverse isochron age (Ma) from all steps: 20.09 ± 0.06 Initial ^{40}Ar/^{36}Ar = 302.8 ± 0.4 MSWD: 5.01

Total gas age (Ma): 22.02 ± 0.15

Laser output[a]	^{40}Ar/^{39}Ar		^{37}Ar/^{39}Ar		^{36}Ar/^{39}Ar (x10^{-3})		K/Ca	^{40}Ar* (%)	^{39}Ar$_K$ fraction (%)	^{40}Ar*/^{39}Ar$_K$		Age(±1s) (Ma)	

Sample ID: MEK-1 kf *Laboratory ID: 1257* *Irradiation ID: PO-9*

J= (1.9041 ± 0.0026) x 10^{-3}

1.6%	43.98	± 1.20	0.001	± 0.773	105.76	± 3.69	755	28.20	0.25	12.40	± 0.78	42.20	± 2.66
2.0%	12.25	± 0.09	0.00	± 0.11	0.98	± 0.23	5196	97.60	1.71	11.96	± 0.11	40.71	± 0.38
2.2%	11.61	± 0.09	0.00	± 0.11	1.07	± 0.23	5352	97.26	1.76	11.29	± 0.12	38.47	± 0.40
2.4%	11.47	± 0.08	0.00	± 0.09	0.81	± 0.16	7026	97.89	2.32	11.22	± 0.09	38.24	± 0.32
2.6%	11.38	± 0.07	0.00	± 0.06	0.79	± 0.10	10192	97.92	3.37	11.14	± 0.08	37.97	± 0.27
2.8%	11.36	± 0.06	0.02	± 0.04	0.83	± 0.07	31	97.83	6.25	11.11	± 0.06	37.85	± 0.21
2.9%	11.39	± 0.04	0.00	± 0.02	0.19	± 0.04	232	99.52	9.34	11.33	± 0.04	38.60	± 0.14
3.0%	11.27	± 0.03	0.07	± 0.02	0.33	± 0.03	7	99.18	12.07	11.18	± 0.03	38.07	± 0.12
3.1%	11.21	± 0.03	0.00	± 0.02	0.03	± 0.04	301	99.92	10.21	11.20	± 0.03	38.15	± 0.12
3.2%	11.40	± 0.05	0.02	± 0.05	0.11	± 0.11	33	99.72	3.73	11.37	± 0.06	38.73	± 0.22
3.4%	11.30	± 0.08	0.04	± 0.06	0.41	± 0.14	14	98.96	3.06	11.19	± 0.09	38.11	± 0.30
3.7%	11.27	± 0.07	0.00	± 0.05	0.20	± 0.11	10918	99.46	3.62	11.21	± 0.08	38.18	± 0.26
4.0%	11.20	± 0.05	0.00	± 0.04	0.00	± 0.09	12495	100.00	4.15	11.20	± 0.06	38.14	± 0.20
4.3%	11.30	± 0.04	0.000	± 0.013	0.12	± 0.02	44741	99.67	14.86	11.26	± 0.04	38.35	± 0.16
4.6%	11.34	± 0.05	0.014	± 0.008	0.10	± 0.02	37	99.75	23.31	11.31	± 0.05	38.53	± 0.17

Plateau age (Ma): **38.31 ± 0.07** Plateau steps: 9th to 15th ^{39}Ar %: 62.9 %

Normal isochron age (Ma) from plateau: 38.23 ± 0.15 Initial ^{40}Ar/^{36}Ar = 246.7 ± 250.4 MSWD: 0.88

Inverse isochron age (Ma) from plateau: 38.04 ± 0.15 Initial ^{40}Ar/^{36}Ar = 970.9 ± 404.0 MSWD: 1.12

Total gas age (Ma): 38.27 ± 0.06

Sample ID: GE-7 gm *Laboratory ID: 1290* *Irradiation ID: PO-10*

J= (1.8822 ± 0.0043) x 10^{-3}

Laser output^{a}	^{40}Ar/^{39}Ar		^{37}Ar/^{39}Ar		^{36}Ar/^{39}Ar (x10^{-3})		K/Ca	^{40}Ar* (%)	^{39}Ar$_K$ fraction (%)	^{40}Ar*/^{39}Ar$_K$		Age(±1s) (Ma)	
1.4%	242.93	± 4.05	1.78	± 0.70	787.60	± 13.94	0.30	3.26	0.63	7.93	± 1.79	26.80	± 6.06
1.7%	45.24	± 0.47	2.62	± 0.22	108.42	± 1.30	0.20	28.92	2.92	13.11	± 0.33	44.08	± 1.10
2.2%	17.78	± 0.19	2.22	± 0.13	19.14	± 0.37	0.24	68.88	5.32	12.26	± 0.17	41.26	± 0.59
2.4%	14.60	± 0.12	1.81	± 0.09	10.43	± 0.17	0.29	79.68	11.03	11.65	± 0.12	39.21	± 0.40
2.6%	14.42	± 0.08	1.37	± 0.07	9.69	± 0.13	0.38	80.71	14.34	11.65	± 0.09	39.23	± 0.30
2.8%	15.85	± 0.14	1.12	± 0.11	14.50	± 0.18	0.47	73.26	12.53	11.62	± 0.12	39.14	± 0.42
3.0%	16.99	± 0.13	1.41	± 0.10	17.77	± 0.25	0.37	69.44	9.27	11.81	± 0.13	39.74	± 0.44
3.2%	16.89	± 0.15	1.45	± 0.14	18.68	± 0.24	0.36	67.69	8.69	11.44	± 0.14	38.54	± 0.47
3.5%	18.86	± 0.20	2.22	± 0.12	25.70	± 0.34	0.24	60.29	8.49	11.39	± 0.17	38.36	± 0.58
3.8%	18.38	± 0.10	6.51	± 0.10	27.60	± 0.25	0.08	58.06	12.48	10.72	± 0.10	36.12	± 0.34
4.1%	18.29	± 0.12	11.86	± 0.20	27.07	± 0.26	0.04	61.11	14.28	11.27	± 0.12	37.96	± 0.42

Plateau age (Ma): **39.12 ± 0.17** Plateau steps: 4th to 9th ^{39}Ar %: 64.4 %

Normal isochron age (Ma) from plateau: 39.56 ± 0.49 Initial ^{40}Ar/^{36}Ar = 287.1 ± 9.9 MSWD: 1.04

Inverse isochron age (Ma) from plateau: 39.55 ± 0.49 Initial ^{40}Ar/^{36}Ar = 287.5 ± 9.9 MSWD: 1.06

Total gas age (Ma): 38.65 ± 0.14

Sample ID: GE-1 gm *Laboratory ID: 1291* *Irradiation ID: PO-10*

J= (1.8789 ± 0.0043) x 10^{-3}

Laser output^{a}	^{40}Ar/^{39}Ar		^{37}Ar/^{39}Ar		^{36}Ar/^{39}Ar (x10^{-3})		K/Ca	^{40}Ar* (%)	^{39}Ar$_K$ fraction (%)	^{40}Ar*/^{39}Ar$_K$		Age(±1s) (Ma)	
1.4%	1006.5	± 13.0	10.41	± 2.61	3360.6	± 54.5	0.05	0.40	0.16	4.03	± 11.68	13.64	± 39.53
1.7%	190.96	± 3.44	5.87	± 0.91	593.5	± 12.8	0.09	7.45	0.53	14.29	± 2.85	47.90	± 9.54
2.0%	70.99	± 1.24	3.75	± 0.53	221.50	± 5.59	0.14	7.27	0.97	5.18	± 1.34	17.50	± 4.52
2.2%	31.29	± 0.48	4.27	± 0.25	83.23	± 2.02	0.12	21.70	1.96	6.81	± 0.58	22.99	± 1.98
2.4%	20.56	± 0.19	2.81	± 0.15	50.81	± 1.03	0.19	27.33	3.85	5.63	± 0.30	19.03	± 1.03
2.6%	16.26	± 0.11	2.34	± 0.11	33.73	± 0.26	0.22	39.24	8.88	6.39	± 0.11	21.58	± 0.38
2.8%	11.06	± 0.09	1.67	± 0.06	16.66	± 0.15	0.31	56.27	22.63	6.23	± 0.07	21.05	± 0.23
3.0%	7.07	± 0.05	1.28	± 0.04	4.64	± 0.05	0.41	81.87	32.06	5.79	± 0.05	19.56	± 0.17
3.2%	7.45	± 0.05	1.22	± 0.06	5.63	± 0.20	0.43	78.77	13.29	5.87	± 0.07	19.85	± 0.26
3.5%	10.25	± 0.08	3.35	± 0.14	16.32	± 0.49	0.16	55.13	6.31	5.67	± 0.16	19.15	± 0.55
3.8%	11.73	± 0.14	9.17	± 0.25	22.54	± 0.66	0.06	49.00	3.87	5.79	± 0.23	19.55	± 0.79
4.3%	11.11	± 0.09	10.70	± 0.28	20.71	± 0.58	0.05	52.21	5.48	5.85	± 0.19	19.75	± 0.64

Plateau age (Ma): **19.62 ± 0.13** Plateau steps: 8th to 12th ^{39}Ar %: 61.0 %

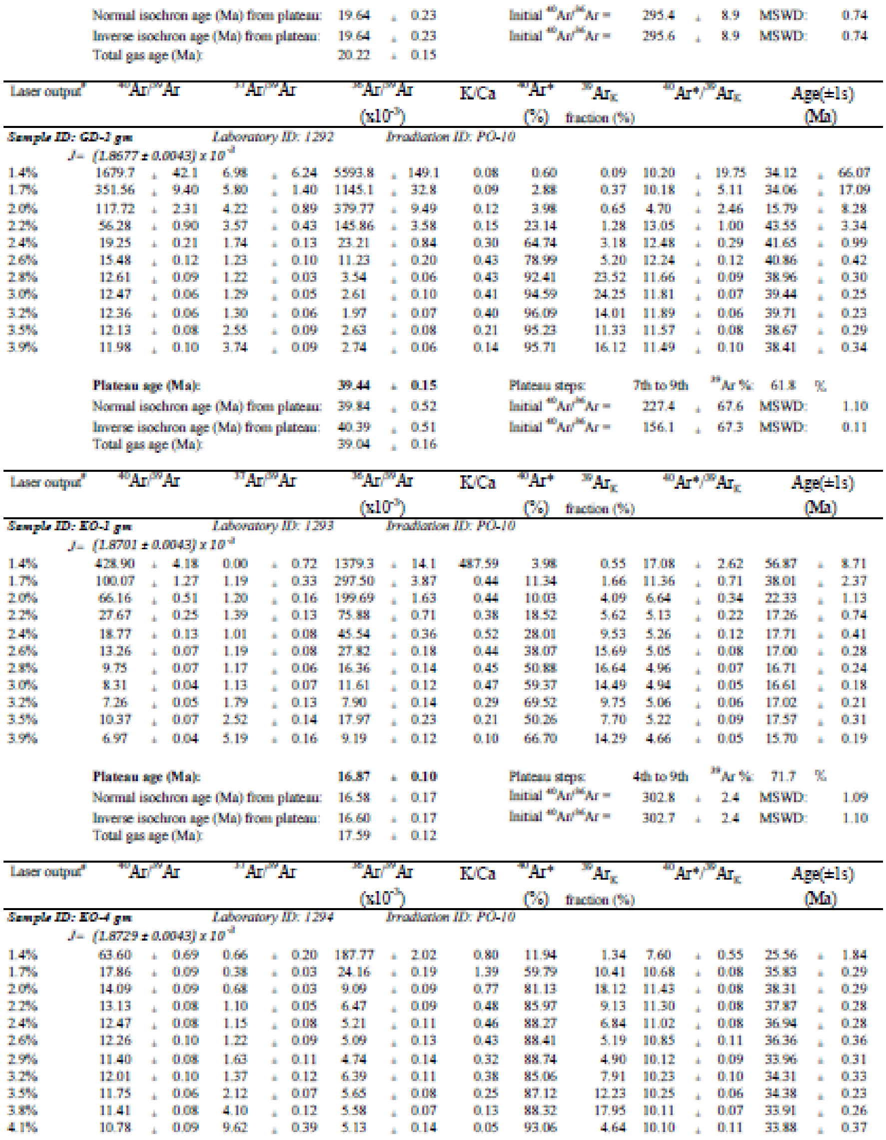

Normal isochron age (Ma) from plateau: 19.64 ± 0.23 Initial ^{40}Ar/^{36}Ar = 295.4 ± 8.9 MSWD: 0.74
Inverse isochron age (Ma) from plateau: 19.64 ± 0.23 Initial ^{40}Ar/^{36}Ar = 295.6 ± 8.9 MSWD: 0.74
Total gas age (Ma): 20.22 ± 0.15

Laser output[#]	^{40}Ar/^{39}Ar		^{37}Ar/^{39}Ar		^{36}Ar/^{39}Ar (x10^{-3})		K/Ca	^{40}Ar* (%)	^{39}Ar$_K$ fraction (%)	^{40}Ar*/^{39}Ar$_K$		Age(±1s) (Ma)	
Sample ID: GD-2 gm			*Laboratory ID: 1292*			*Irradiation ID: PO-10*							
J= (1.8677 ± 0.0043) x 10^{-3}													
1.4%	1679.7	± 42.1	6.98	± 6.24	5593.8	± 149.1	0.08	0.60	0.09	10.20	± 19.75	34.12	± 66.07
1.7%	351.56	± 9.40	5.80	± 1.40	1145.1	± 32.8	0.09	2.88	0.37	10.18	± 5.11	34.06	± 17.09
2.0%	117.72	± 2.31	4.22	± 0.89	379.77	± 9.49	0.12	3.98	0.65	4.70	± 2.46	15.79	± 8.28
2.2%	56.28	± 0.90	3.57	± 0.43	145.86	± 3.58	0.15	23.14	1.28	13.05	± 1.00	43.55	± 3.34
2.4%	19.25	± 0.21	1.74	± 0.13	23.21	± 0.84	0.30	64.74	3.18	12.48	± 0.29	41.65	± 0.99
2.6%	15.48	± 0.12	1.23	± 0.10	11.23	± 0.20	0.43	78.99	5.20	12.24	± 0.12	40.86	± 0.42
2.8%	12.61	± 0.09	1.22	± 0.03	3.54	± 0.06	0.43	92.41	23.52	11.66	± 0.09	38.96	± 0.30
3.0%	12.47	± 0.06	1.29	± 0.05	2.61	± 0.10	0.41	94.59	24.25	11.81	± 0.07	39.44	± 0.25
3.2%	12.36	± 0.06	1.30	± 0.06	1.97	± 0.07	0.40	96.09	14.01	11.89	± 0.06	39.71	± 0.23
3.5%	12.13	± 0.08	2.55	± 0.09	2.63	± 0.08	0.21	95.23	11.33	11.57	± 0.08	38.67	± 0.29
3.9%	11.98	± 0.10	3.74	± 0.09	2.74	± 0.06	0.14	95.71	16.12	11.49	± 0.10	38.41	± 0.34

Plateau age (Ma): **39.44 ± 0.15** Plateau steps: 7th to 9th ^{39}Ar %: 61.8 %
Normal isochron age (Ma) from plateau: 39.84 ± 0.52 Initial ^{40}Ar/^{36}Ar = 227.4 ± 67.6 MSWD: 1.10
Inverse isochron age (Ma) from plateau: 40.39 ± 0.51 Initial ^{40}Ar/^{36}Ar = 156.1 ± 67.3 MSWD: 0.11
Total gas age (Ma): 39.04 ± 0.16

Laser output[#]	^{40}Ar/^{39}Ar		^{37}Ar/^{39}Ar		^{36}Ar/^{39}Ar (x10^{-3})		K/Ca	^{40}Ar* (%)	^{39}Ar$_K$ fraction (%)	^{40}Ar*/^{39}Ar$_K$		Age(±1s) (Ma)	
Sample ID: EO-1 gm			*Laboratory ID: 1293*			*Irradiation ID: PO-10*							
J= (1.8701 ± 0.0043) x 10^{-3}													
1.4%	428.90	± 4.18	0.00	± 0.72	1379.3	± 14.1	487.59	3.98	0.55	17.08	± 2.62	56.87	± 8.71
1.7%	100.07	± 1.27	1.19	± 0.33	297.50	± 3.87	0.44	11.34	1.66	11.36	± 0.71	38.01	± 2.37
2.0%	66.16	± 0.51	1.20	± 0.16	199.69	± 1.63	0.44	10.03	4.09	6.64	± 0.34	22.33	± 1.13
2.2%	27.67	± 0.25	1.39	± 0.13	75.88	± 0.71	0.38	18.52	5.62	5.13	± 0.22	17.26	± 0.74
2.4%	18.77	± 0.13	1.01	± 0.08	45.54	± 0.36	0.52	28.01	9.53	5.26	± 0.12	17.71	± 0.41
2.6%	13.26	± 0.07	1.19	± 0.08	27.82	± 0.18	0.44	38.07	15.69	5.05	± 0.08	17.00	± 0.28
2.8%	9.75	± 0.07	1.17	± 0.06	16.36	± 0.14	0.45	50.88	16.64	4.96	± 0.07	16.71	± 0.24
3.0%	8.31	± 0.04	1.13	± 0.07	11.61	± 0.12	0.47	59.37	14.49	4.94	± 0.05	16.61	± 0.18
3.2%	7.26	± 0.05	1.79	± 0.13	7.90	± 0.14	0.29	69.52	9.75	5.06	± 0.06	17.02	± 0.21
3.5%	10.37	± 0.07	2.52	± 0.14	17.97	± 0.23	0.21	50.26	7.70	5.22	± 0.09	17.57	± 0.31
3.9%	6.97	± 0.04	5.19	± 0.16	9.19	± 0.12	0.10	66.70	14.29	4.66	± 0.05	15.70	± 0.19

Plateau age (Ma): **16.87 ± 0.10** Plateau steps: 4th to 9th ^{39}Ar %: 71.7 %
Normal isochron age (Ma) from plateau: 16.58 ± 0.17 Initial ^{40}Ar/^{36}Ar = 302.8 ± 2.4 MSWD: 1.09
Inverse isochron age (Ma) from plateau: 16.60 ± 0.17 Initial ^{40}Ar/^{36}Ar = 302.7 ± 2.4 MSWD: 1.10
Total gas age (Ma): 17.59 ± 0.12

Laser output[#]	^{40}Ar/^{39}Ar		^{37}Ar/^{39}Ar		^{36}Ar/^{39}Ar (x10^{-3})		K/Ca	^{40}Ar* (%)	^{39}Ar$_K$ fraction (%)	^{40}Ar*/^{39}Ar$_K$		Age(±1s) (Ma)	
Sample ID: EO-4 gm			*Laboratory ID: 1294*			*Irradiation ID: PO-10*							
J= (1.8729 ± 0.0043) x 10^{-3}													
1.4%	63.60	± 0.69	0.66	± 0.20	187.77	± 2.02	0.80	11.94	1.34	7.60	± 0.55	25.56	± 1.84
1.7%	17.86	± 0.09	0.38	± 0.03	24.16	± 0.19	1.39	59.79	10.41	10.68	± 0.08	35.83	± 0.29
2.0%	14.09	± 0.09	0.68	± 0.03	9.09	± 0.09	0.77	81.13	18.12	11.43	± 0.08	38.31	± 0.29
2.2%	13.13	± 0.08	1.10	± 0.05	6.47	± 0.09	0.48	85.97	9.13	11.30	± 0.08	37.87	± 0.28
2.4%	12.47	± 0.08	1.15	± 0.08	5.21	± 0.11	0.46	88.27	6.84	11.02	± 0.08	36.94	± 0.28
2.6%	12.26	± 0.10	1.22	± 0.09	5.09	± 0.13	0.43	88.41	5.19	10.85	± 0.11	36.36	± 0.36
2.9%	11.40	± 0.08	1.63	± 0.11	4.74	± 0.14	0.32	88.74	4.90	10.12	± 0.09	33.96	± 0.31
3.2%	12.01	± 0.10	1.37	± 0.12	6.39	± 0.11	0.38	85.06	7.91	10.23	± 0.10	34.31	± 0.33
3.5%	11.75	± 0.06	2.12	± 0.07	5.65	± 0.08	0.25	87.12	12.23	10.25	± 0.06	34.38	± 0.23
3.8%	11.41	± 0.08	4.10	± 0.12	5.58	± 0.07	0.13	88.32	17.95	10.11	± 0.07	33.91	± 0.26
4.1%	10.78	± 0.09	9.62	± 0.39	5.13	± 0.14	0.05	93.06	4.64	10.10	± 0.11	33.88	± 0.37

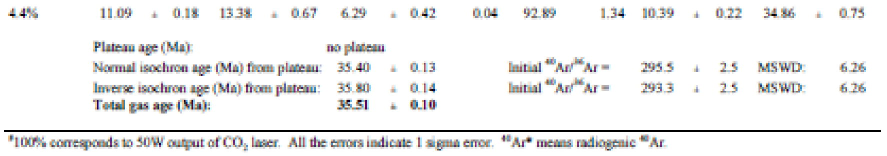

4.4%	11.09	± 0.18	13.38	± 0.67	6.29	± 0.42	0.04	92.89	1.34	10.39	± 0.22	34.86	± 0.75

Plateau age (Ma): no plateau
Normal isochron age (Ma) from plateau: 35.40 ± 0.13 Initial ^{40}Ar/^{36}Ar = 295.5 ± 2.5 MSWD: 6.26
Inverse isochron age (Ma) from plateau: 35.80 ± 0.14 Initial ^{40}Ar/^{36}Ar = 293.3 ± 2.5 MSWD: 6.26
Total gas age (Ma): **35.51 ± 0.10**

[#] 100% corresponds to 50W output of CO_2 laser. All the errors indicate 1 sigma error. ^{40}Ar* means radiogenic ^{40}Ar.

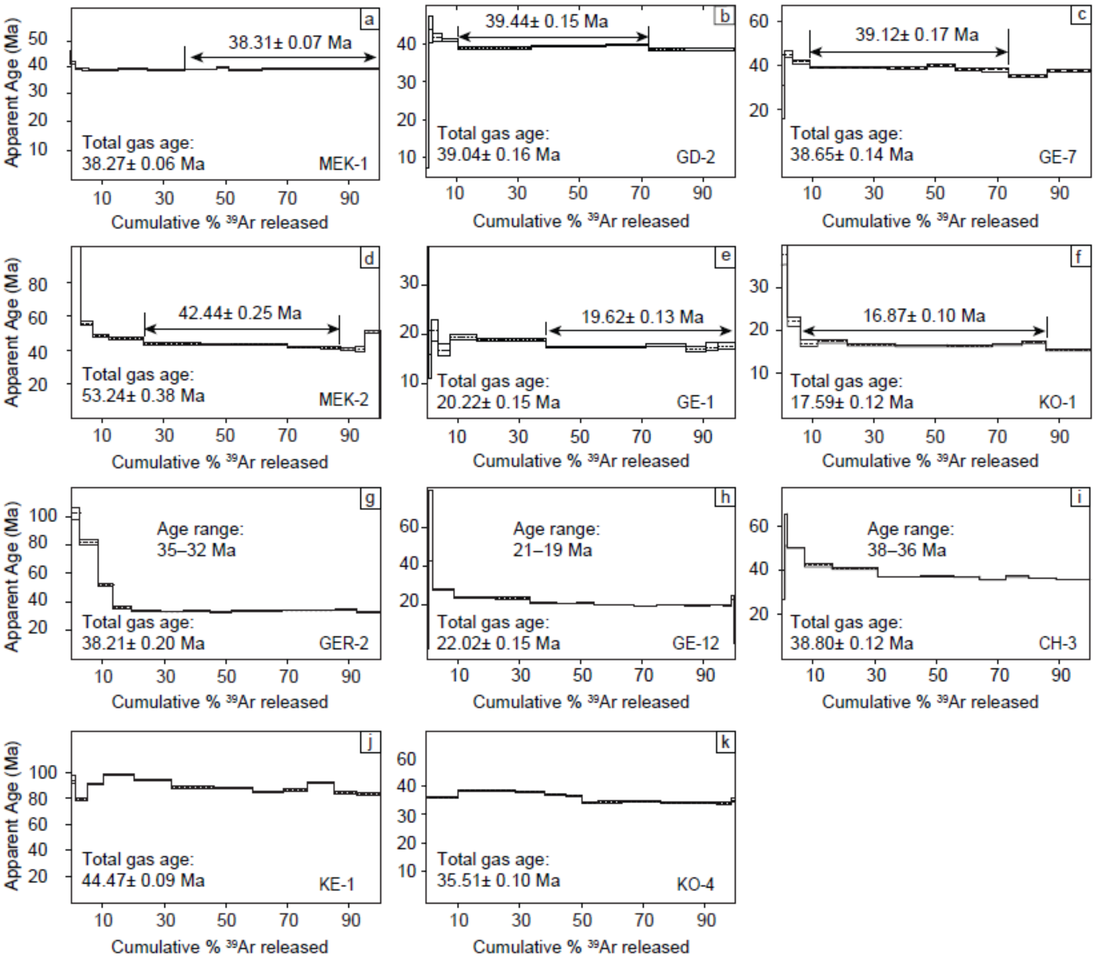

Figure 3: Representative ^{40}Ar/^{39}Ar-dating results from basaltic flows sampled for paleomagnetic analyses across the Gidole-Chencha Horst. (a–f) Plateau ages obtained for samples from consecutive heating experiments; (g–i) age range for the samples estimated from relatively long flat age patterns (Schaen et al., 2020), occupying >65% of the fraction of ^{39}Ar release. The total gas age is shown for all samples.

3.2 Paleomagnetic results

Based on our new ^{40}Ar/^{39}Ar data presented above, existing regional geochronologic information (e.g., Davidson and Rex, 1980; Davidson, 1983; Ebinger et al., 1993, 2000; George, 1998; George and Rogers, 2002; Bonini et al., 2005; Rooney et al., 2010), as well as detailed petrographic studies (e.g., Steiner et al., 2021), we gathered the sampled paleomagnetic sites into an Eo–Oligocene age group (45–27 Ma; e.g., Steiner et al., 2021) and a Miocene age group (20–11 Ma). We also established a relative stratigraphic section for the sampled units (Fig. 4).

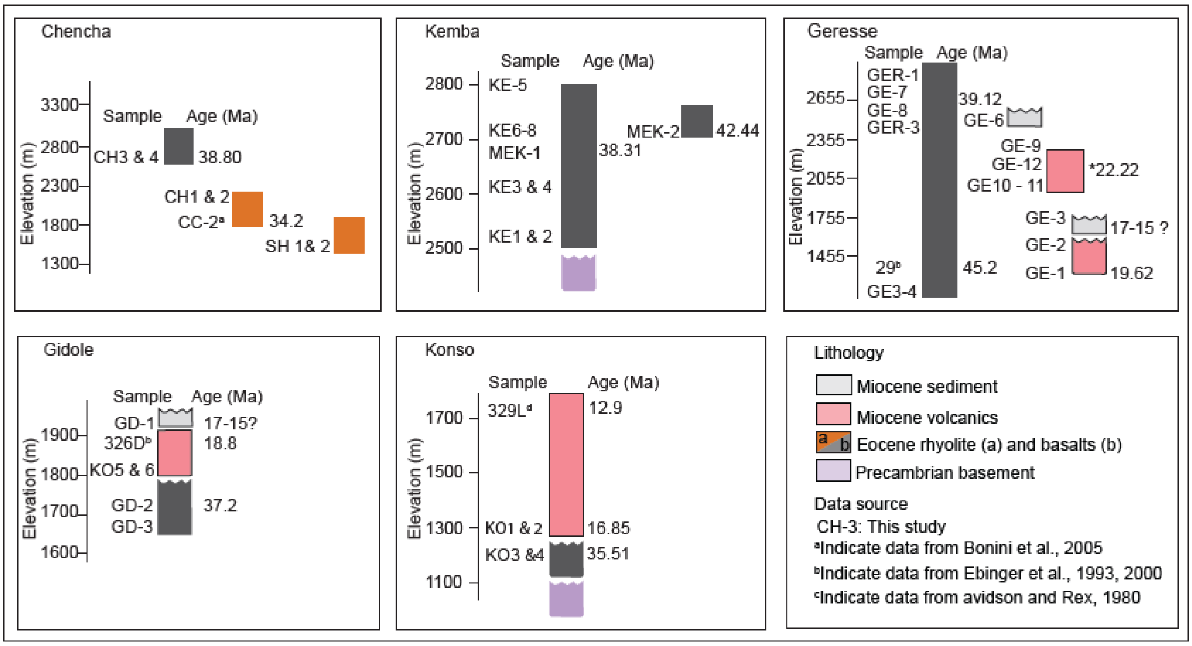

Figure 4: Chronostratigraphic sections for the sampled Chencha, Kemba, Geresse, Gidole and Konso localities. Geochronologic results from our study and regional age information were combined with specific sampling locations for each site and used to establish a relative stratigraphy.

3.2.1 Rock magnetic behavior

The NRM intensities measured prior to the demagnetization experiments provided an average value of 1.1 and 7.1 A/m for the Eo–Oligocene and Miocene rocks, respectively (Fig. 5). The thermal demagnetizations of pilot samples showed limited decay between 0 and 150 °C suggesting goethite does not significantly contribute to the magnetization (Dunlop and Ozdemir, 2007; Figs. 6 and 7). Further thermal decay of demagnetizations showed simple univectorial decay of most of the NRM between 400 and 600 °C typical of volcanic rocks with strong magnetizations dominated by titanomagnetite. Only about four of the pilot samples (Figs. 6b, f and 7d) exhibit a final decay between 600 and 680 °C, suggesting the presence of hematite or its formation during thermal demagnetization. Comparison with thermomagnetic runs and AF demagnetizations provide further insight. Thermomagnetic runs (Fig. 8) mainly display most of the bulk susceptibility decrease within 400 to 600 °C, sometimes preceded by a typical of Hopkinson's peak, and mostly reversible heating and cooling curves. These are typical of magnetite and/or titanomagnetite. Most of the thermomagnetic runs (Fig. 8) exhibit a large drop in susceptibility between 400 and 620°C typical of mineralogies dominated by titanomagnetite. In detail, more than one temperature points between 400 and 600 °C, and between 600 and 620 °C, may document a range of titanomagnetite and some titanohematite. However, the strong susceptibility of these phases may hide the potential presence of other iron oxides such as hematite with much lower susceptibility values. AF demagnetizations of these samples typically show that most of the decay occurred between 10 and 60 mT, which is characteristic of magnetite and titanomagnetite. In most samples, the magnetization is fully removed at 100 mT, in others, a significant residual stronger coercivity remanence is preserved above 100 mT (see in particular the Eo–Oligocene and Miocene volcanics and sediments in Figs. 6, and 7). This stronger coercivity is not likely due to goethite not being apparent in the thermal demagnetization. It is rather interpreted to reflect variable occurrences of hematite in the samples. The directions of this high-temperature component, when present in the pilot thermal demagnetizations (Fig. 6 and 7), are indistinguishable from the Characteristic Remanent Magnetization (ChRM) direction defined within 400–600 °C. Further rock-magnetic experiments would be required to better define the precise nature of this occasional high-temperature component. However, this is not necessary for the purpose of our study since this high-temperature component, when present, does not affect the orientation of the well-defined characteristic component carrying most of the magnetization. A more troubling behavior was found upon AF demagnetizations in about 10% and 15% of the Miocene and Eo–Oligocene samples, respectively. In these samples, most of the magnetization was removed after low AF demagnetization within 0-10 mT. This low coercivity may be interpreted to be related to Ti-rich titanomagnetite, which is often present in volcanic rocks outcropping in the region (Dunlop and Ozdemir, 2007; Nugsse et al., 2018). These low coercivity samples have more scattered directions suggesting that some of them have acquired a recent viscous remagnetization not suitable for further tectonic analyses. To simplify the systematic identification and rejection of these unreliable samples with lower coercivities, the Median Destructive Field (MDF), defined as the applied AF field removing half of the initial magnetization, was used to conservatively reject from further analyses all samples with MDF < 10 mT (Table 2 and Fig. 6c). The three Miocene clastic sedimentary sites had similar behaviors to the surrounding basalts with most of the ChRM demagnetized between 400–600 °C and 20–60 mT (e.g., Fig 7e and f). Given the simple behavior of most basaltic and clastic pilot samples with a Characteristic Remanent Magnetization and well-defined by AF treatment showing univectorial decay towards the origin, this procedure was applied to the bulk of the samples (see Methods). The systematic rejection of samples with low MDF values resulted in discarding five sites that exhibited these behaviors (Table 2).

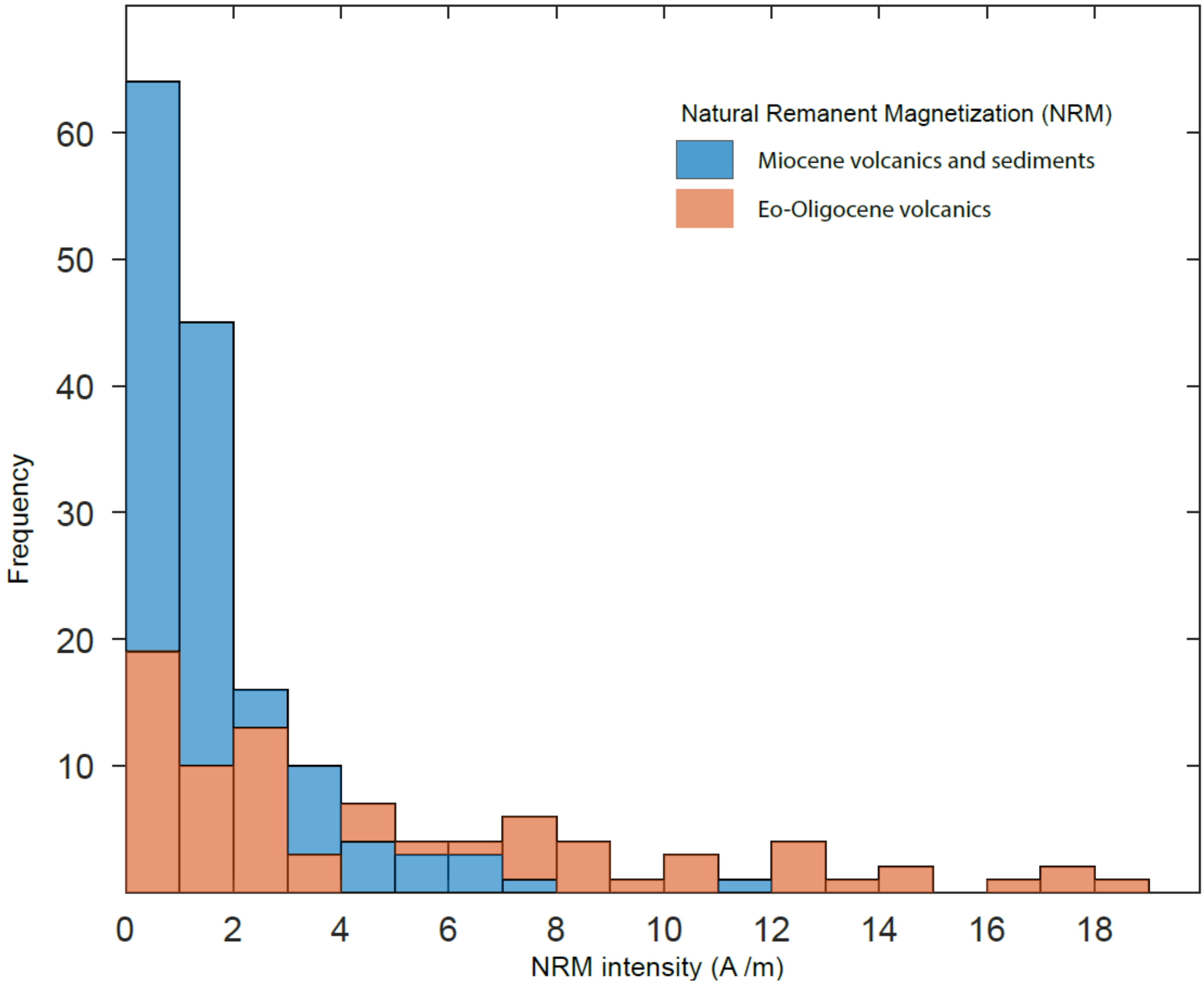

Figure 5: Histogram of NRM for the Eo–Oligocene volcanics and the Miocene volcanics and sediments.

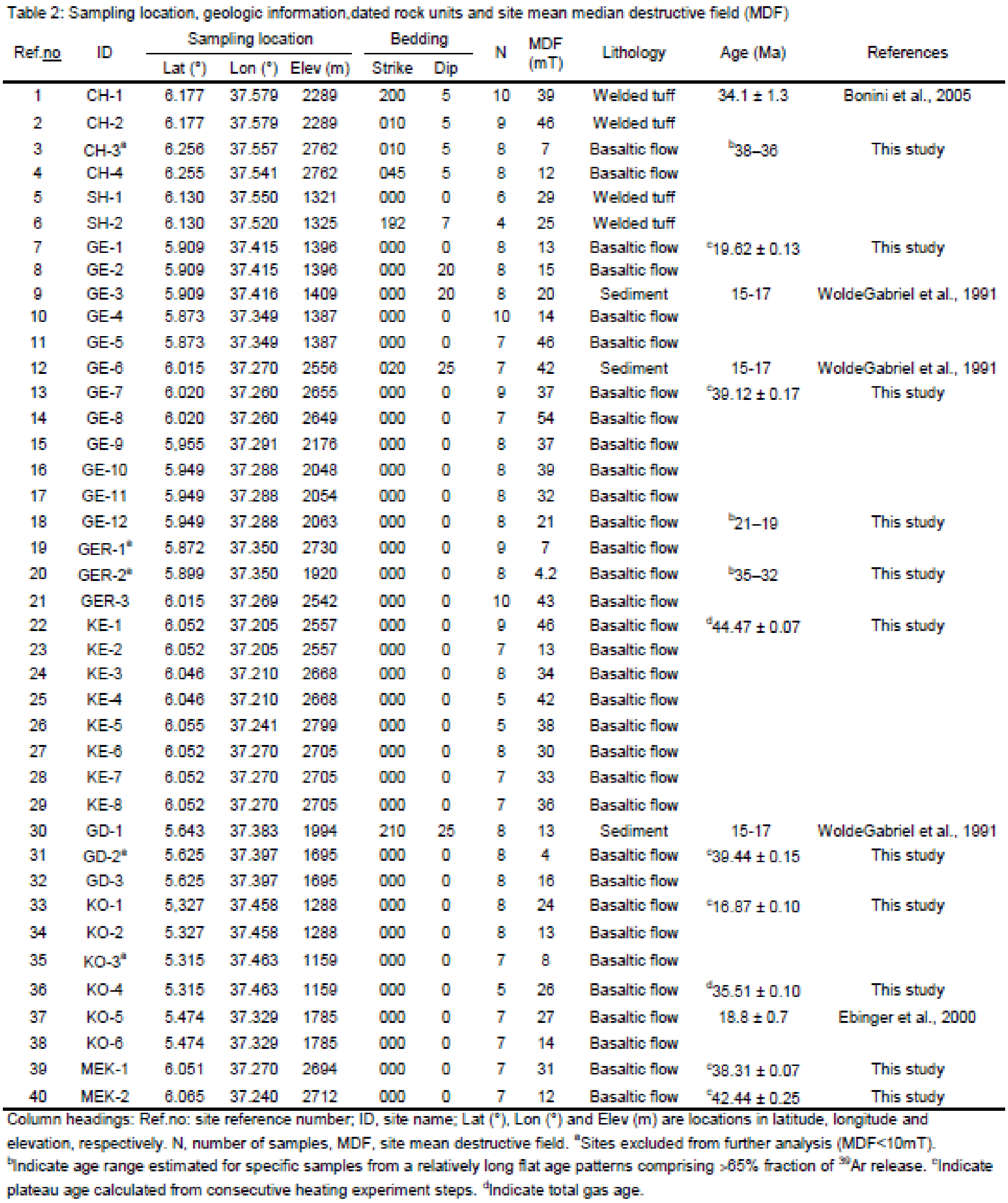

Table 2: Sampling location, geologic information,dated rock units and site mean median destructive field (MDF)

Ref.no	ID	Sampling location			Bedding		N	MDF (mT)	Lithology	Age (Ma)	References
		Lat (°)	Lon (°)	Elev (m)	Strike	Dip					
1	CH-1	6.177	37.579	2289	200	5	10	39	Welded tuff	34.1 ± 1.3	Bonini et al., 2005
2	CH-2	6.177	37.579	2289	010	5	9	46	Welded tuff		
3	CH-3^{a}	6.256	37.557	2762	010	5	8	7	Basaltic flow	^{b}38–36	This study
4	CH-4	6.255	37.541	2762	045	5	8	12	Basaltic flow		
5	SH-1	6.130	37.550	1321	000	0	6	29	Welded tuff		
6	SH-2	6.130	37.520	1325	192	7	4	25	Welded tuff		
7	GE-1	5.909	37.415	1396	000	0	8	13	Basaltic flow	^{c}19.62 ± 0.13	This study
8	GE-2	5.909	37.415	1396	000	20	8	15	Basaltic flow		
9	GE-3	5.909	37.416	1409	000	20	8	20	Sediment	15-17	WoldeGabriel et al., 1991
10	GE-4	5.873	37.349	1387	000	0	10	14	Basaltic flow		
11	GE-5	5.873	37.349	1387	000	0	7	46	Basaltic flow		
12	GE-6	6.015	37.270	2556	020	25	7	42	Sediment	15-17	WoldeGabriel et al., 1991
13	GE-7	6.020	37.260	2655	000	0	9	37	Basaltic flow	^{c}39.12 ± 0.17	This study
14	GE-8	6.020	37.260	2649	000	0	7	54	Basaltic flow		
15	GE-9	5,955	37.291	2176	000	0	8	37	Basaltic flow		
16	GE-10	5.949	37.288	2048	000	0	8	39	Basaltic flow		
17	GE-11	5.949	37.288	2054	000	0	8	32	Basaltic flow		
18	GE-12	5.949	37.288	2063	000	0	8	21	Basaltic flow	^{b}21–19	This study
19	GER-1^{a}	5.872	37.350	2730	000	0	9	7	Basaltic flow		
20	GER-2^{a}	5.899	37.350	1920	000	0	8	4.2	Basaltic flow	^{b}35–32	This study
21	GER-3	6.015	37.269	2542	000	0	10	43	Basaltic flow		
22	KE-1	6.052	37.205	2557	000	0	9	46	Basaltic flow	^{d}44.47 ± 0.07	This study
23	KE-2	6.052	37.205	2557	000	0	7	13	Basaltic flow		
24	KE-3	6.046	37.210	2668	000	0	8	34	Basaltic flow		
25	KE-4	6.046	37.210	2668	000	0	5	42	Basaltic flow		
26	KE-5	6.055	37.241	2799	000	0	5	38	Basaltic flow		
27	KE-6	6.052	37.270	2705	000	0	8	30	Basaltic flow		
28	KE-7	6.052	37.270	2705	000	0	7	33	Basaltic flow		
29	KE-8	6.052	37.270	2705	000	0	7	36	Basaltic flow		
30	GD-1	5.643	37.383	1994	210	25	8	13	Sediment	15-17	WoldeGabriel et al., 1991
31	GD-2^{a}	5.625	37.397	1695	000	0	8	4	Basaltic flow	^{c}39.44 ± 0.15	This study
32	GD-3	5.625	37.397	1695	000	0	8	16	Basaltic flow		
33	KO-1	5,327	37.458	1288	000	0	8	24	Basaltic flow	^{c}16.87 ± 0.10	This study
34	KO-2	5.327	37.458	1288	000	0	8	13	Basaltic flow		
35	KO-3^{a}	5.315	37.463	1159	000	0	7	8	Basaltic flow		
36	KO-4	5.315	37.463	1159	000	0	5	26	Basaltic flow	^{d}35.51 ± 0.10	This study
37	KO-5	5.474	37.329	1785	000	0	7	27	Basaltic flow	18.8 ± 0.7	Ebinger et al., 2000
38	KO-6	5.474	37.329	1785	000	0	7	14	Basaltic flow		
39	MEK-1	6.051	37.270	2694	000	0	7	31	Basaltic flow	^{c}38.31 ± 0.07	This study
40	MEK-2	6.065	37.240	2712	000	0	7	12	Basaltic flow	^{c}42.44 ± 0.25	This study

Column headings: Ref.no: site reference number; ID, site name; Lat (°), Lon (°) and Elev (m) are locations in latitude, longitude and elevation, respectively. N, number of samples, MDF, site mean destructive field. ^{a}Sites excluded from further analysis (MDF<10mT). ^{b}Indicate age range estimated for specific samples from a relatively long flat age patterns comprising >65% fraction of ^{39}Ar release. ^{c}Indicate plateau age calculated from consecutive heating experiment steps. ^{d}Indicate total gas age.

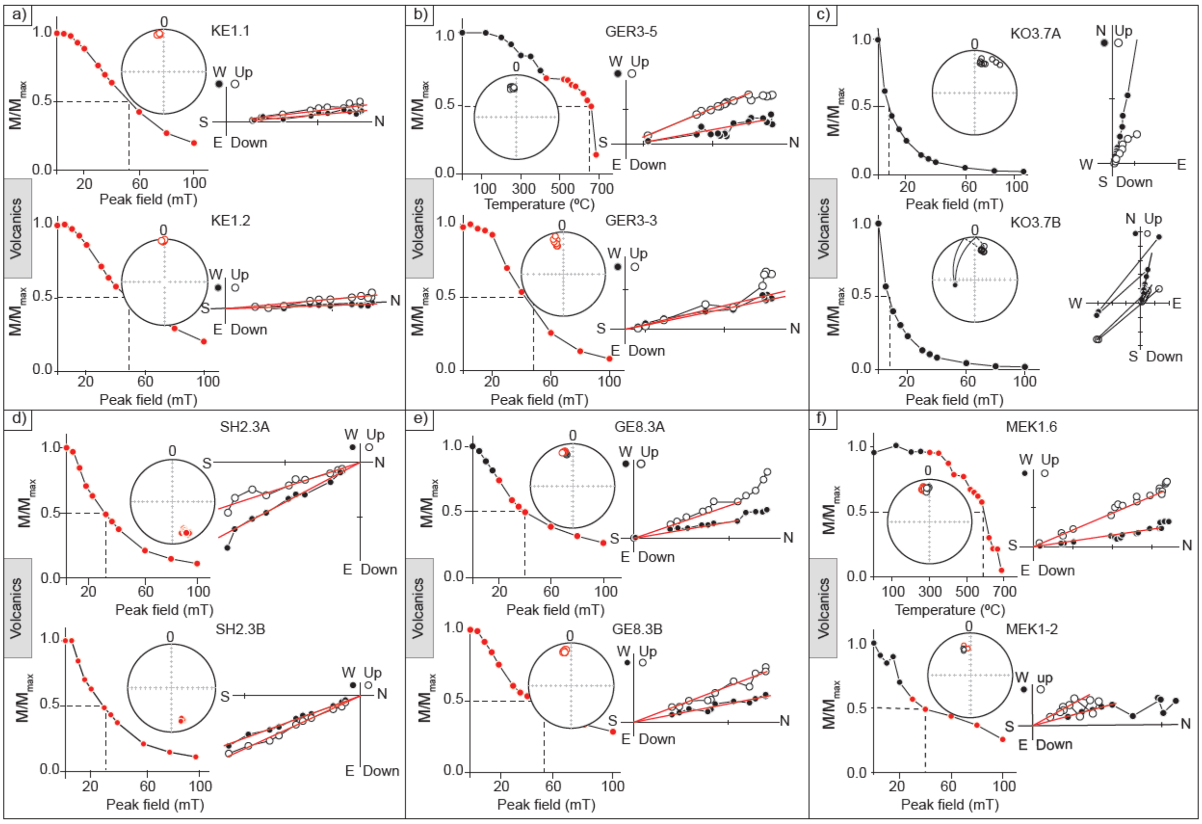

Figure 6. Typical demagnetization behavior of representative specimens obtained from the Eo–Oligocene rocks. Panels (a–f) show stereographic plots, the decay curve exhibiting the median destructive field or temperature (dashed lines), and orthogonal vector end-point diagrams for representative samples demagnetized by AF (a, c, d and e) and thermal treatment (b and f); (c) representative plot for a rejected sample, recording MDF < 10 mT. Red symbols indicate demagnetization steps used for a principal component analysis (red solid line).

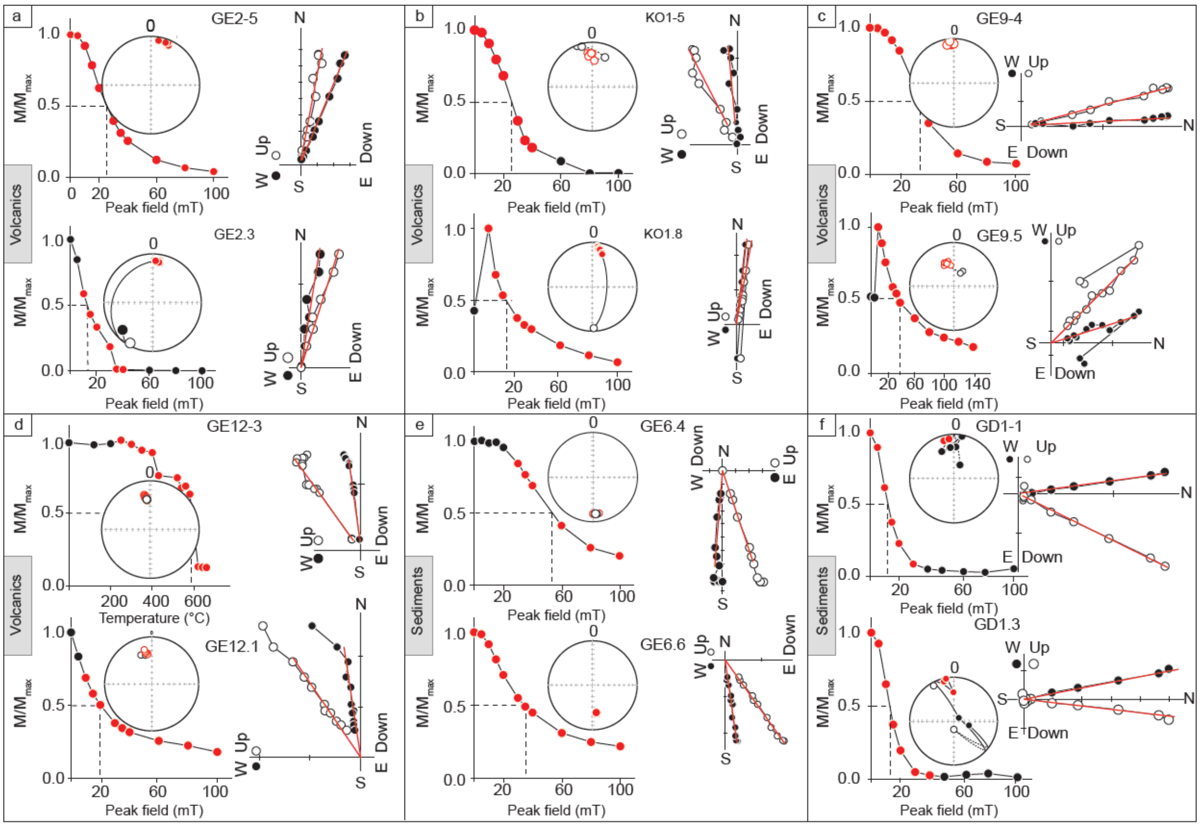

Figure 7. Typical demagnetization behaviors of representative specimens obtained from the Miocene rocks. Panels (a–f) show stereographic plot, the decay curve exhibiting the median destructive field or temperature (dashed lines), and orthogonal vector end-point diagrams for representative samples demagnetized by AF (a–c, e and f) and thermal treatment (d). Red symbols indicate demagnetization steps used for a principal component analysis (red solid line). Most of the specimens exhibit demagnetizations along univectorial paths within 10–60 mT or 400–600 °C (a–e).

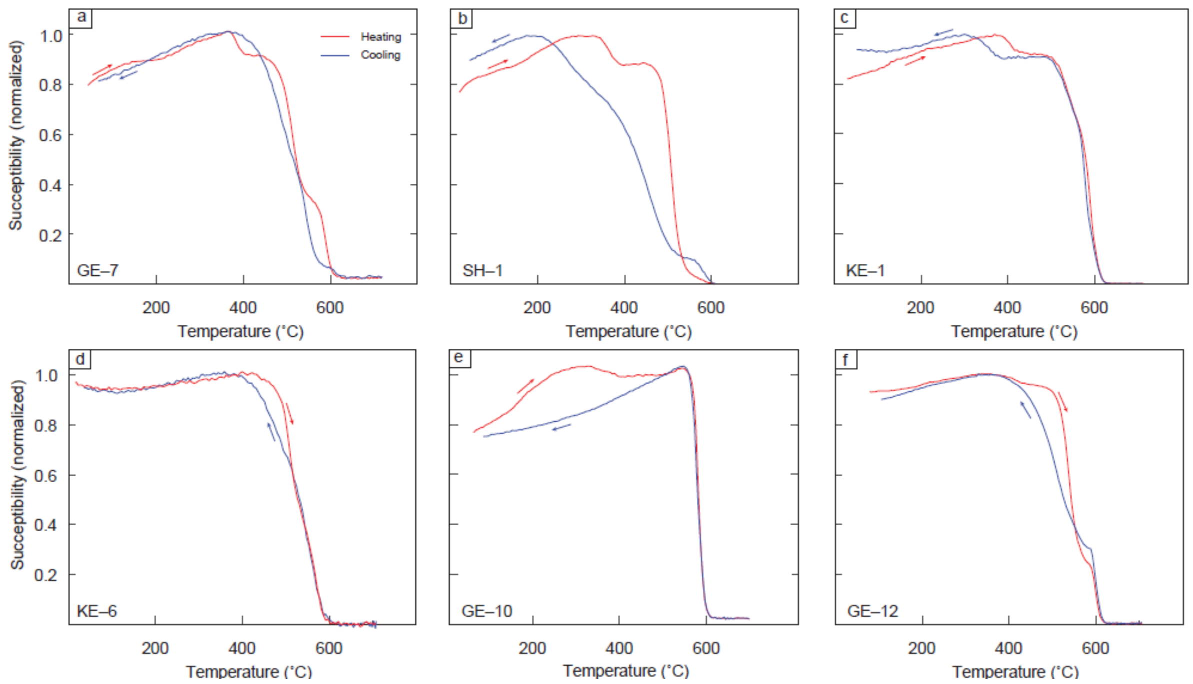

Figure 8: High-temperature thermomagnetic experiment results. Heating (red line) and cooling (blue line) curves for Eo–Oligocene (a–d) and Miocene (e and f) rocks.

3.2.2 Paleomagnetic directions

From the reliable sites, principal component analyses performed on the sample ChRM components yielded well-defined ChRM directions with maximum angular deviations generally well below the threshold value of 15°. These ChRM directions yielded well-defined site-mean directions except for three sites with α_{95} >15° that were discarded (Tables 3 and 4).

In the Eo–Oligocene sites, site means from nearby sites are statistically distinct from each other with 95% confidence. The Eo–Oligocene site-means are generally oriented in normal or reversed polarity orientations after tilt corrections except for three sites widely departing from the mean (Table 3, Fig. 9). These were interpreted as transitional and discarded because the Virtual Geomagnetic Poles (VGP) of these site-means are over 30° from the overall mean paleomagnetic pole of Eo–Oligocene directions (e.g., McFadden et al., 1991). From the remaining sites, a reversals test was positive for the Eo–Oligocene sites based on the overlap within 95% confidence of the mean of the 16 normal and 2 reversed site-mean directions suggesting a primary origin for the ChRM. In addition, the scatter (S=13.2°) in the distribution of the resulting VGPs is comparable to the expected VGP scatter (S=10-20°) at this latitude from modern global records (Johnson et al., 2008; Deenen et al., 2011) and for the Oligocene to Miocene rocks in Kenya (S=13.8-16.5°; Lhuillier and Gilder, 2019), suggesting the dataset is not undersampling the secular variation. Note that some of the scatter may also result from variable amounts of vertical-axis rotations indistinguishable from the secular variation scatter. Distinguishing between these two sources of scatter is challenging and would require a much larger number of sites to be analyzed. However, undersampling of the secular variation with scatter mainly from rotations is considered unlikely given the observed distribution that exhibits scatter both in inclination and declination, the variations in series of flow sampled at the same locality, and the positive reversals test.

From the Miocene localities, nearby site-mean directions are statistically indistinguishable from each other for three successive basaltic flows (GE-10, 11 and GE-12) dated at 19.8 ± 0.1 Ma. Although they are separated by well-developed flow structures, their indistinguishable magnetization directions suggest that the flows are likely the same or that they were emplaced within a short time interval relative to the rate of geomagnetic secular variation. For this reason, ChRM directions from these flows were combined into a single site-mean. The Miocene site-means record mainly normal polarity directions, except for the samples from site GE-6, which was obtained from sedimentary rock recording both normal and reversed geomagnetic polarity (Table 4). The mean normal direction of Miocene sites is clearly antipodal to this single reversed direction suggesting a primary signal, but the latter being alone prevents us from performing a formal reversals test. The observed scatter (S=18.4) in the distribution of the VGPs derived from these sites is, despite the limited number of sites (N=9), also comparable to the expected VGP scatter at this age and latitude (Johnson et al., 2008; Lhuillier and Gilder, 2019).

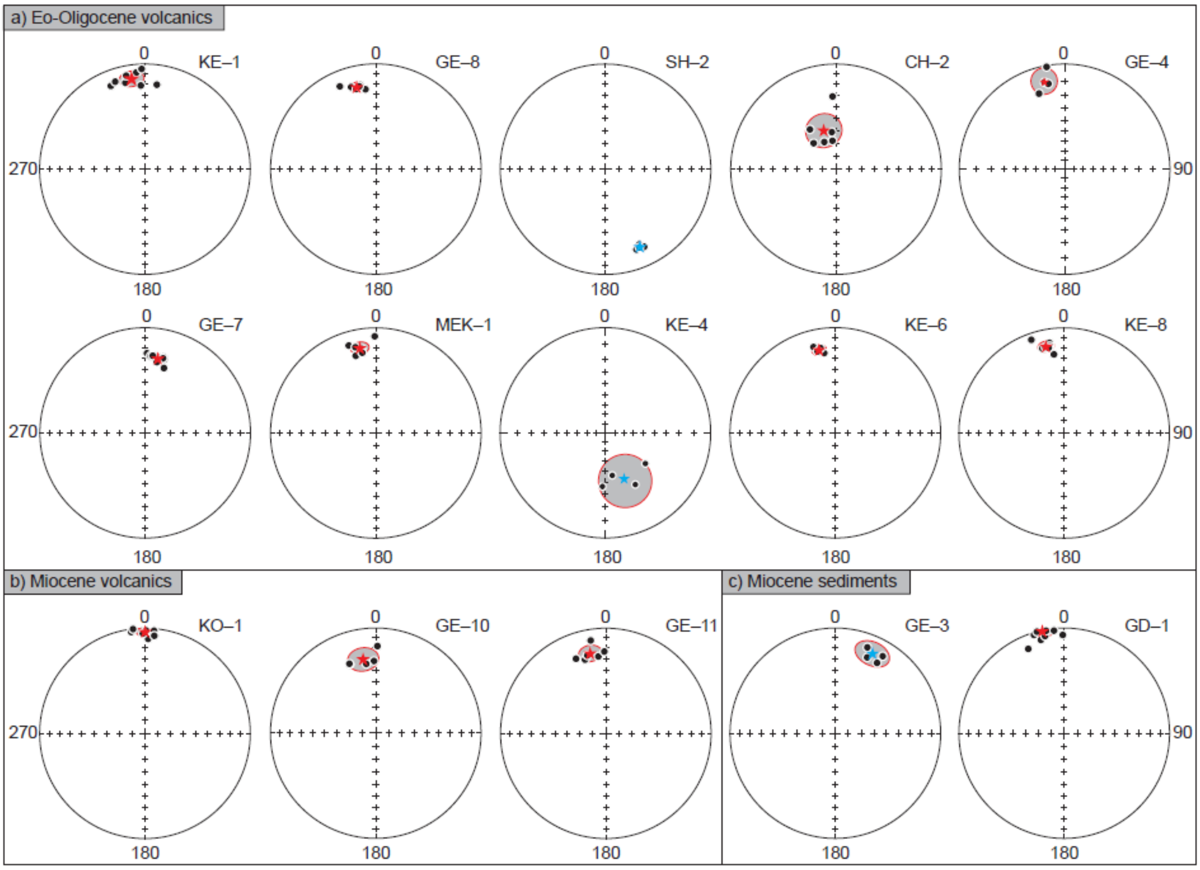

Figure 9: Representative stereoplots of sample ChRM directions at various sites for the Eo–Oligocene volcanics (a) and Miocene volcanics (b) and sediments (c). Site mean directions with 95% (α_{95}) confidence interval are indicated with a star symbol (red and light blue indicate negative and positive inclinations, respectively). Transitional directions SH-2 and KE-4 were excluded when computing an overall mean paleomagnetic direction for the Eo–Oligocene volcanics.

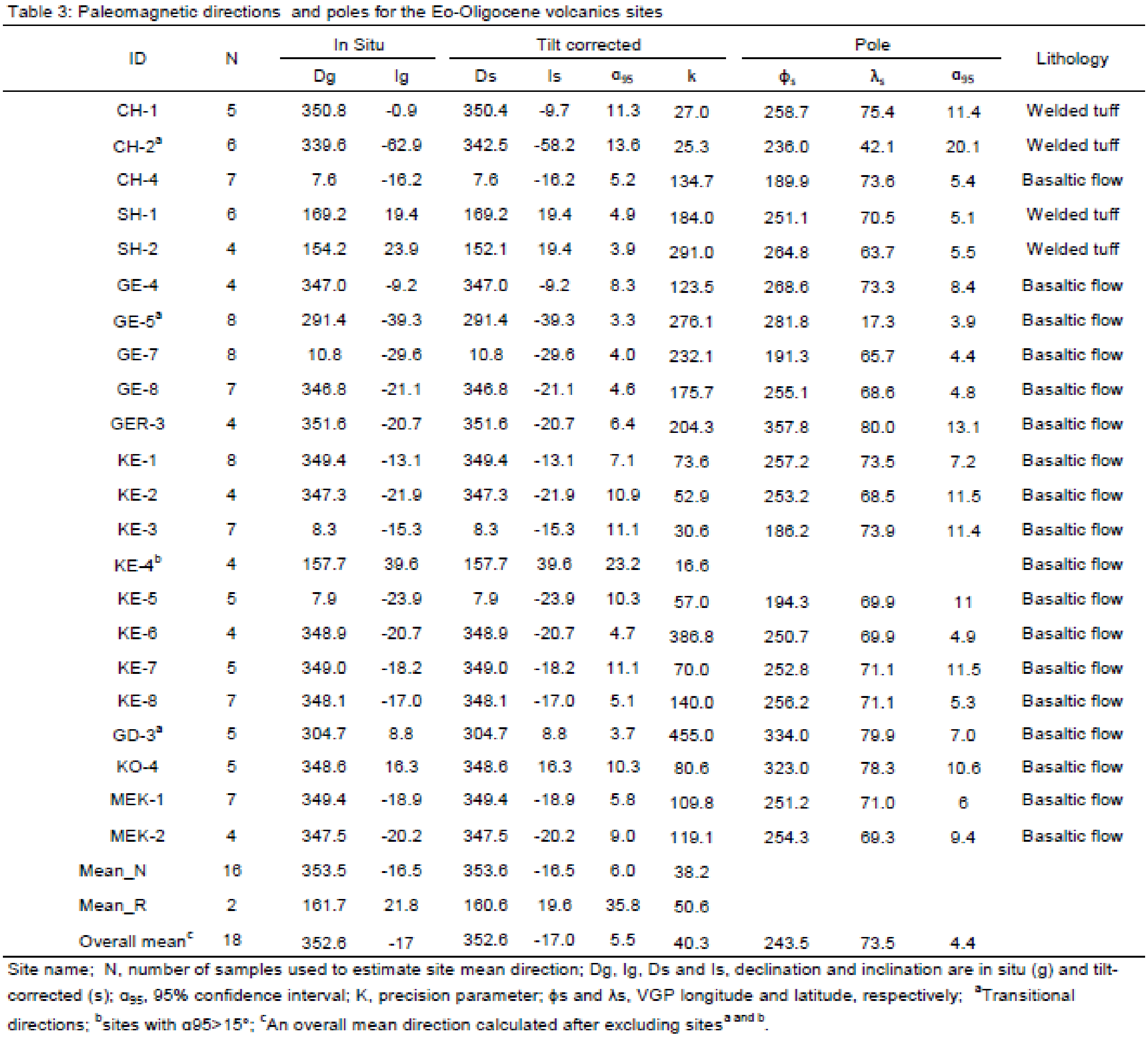

Table 3: Paleomagnetic directions and poles for the Eo-Oligocene volcanics sites

ID	N	In Situ		Tilt corrected				Pole			Lithology
		Dg	Ig	Ds	Is	α_{95}	k	ϕ_s	λ_s	α_{95}	
CH-1	5	350.8	-0.9	350.4	-9.7	11.3	27.0	258.7	75.4	11.4	Welded tuff
CH-2[a]	6	339.6	-62.9	342.5	-58.2	13.6	25.3	236.0	42.1	20.1	Welded tuff
CH-4	7	7.6	-16.2	7.6	-16.2	5.2	134.7	189.9	73.6	5.4	Basaltic flow
SH-1	6	169.2	19.4	169.2	19.4	4.9	184.0	251.1	70.5	5.1	Welded tuff
SH-2	4	154.2	23.9	152.1	19.4	3.9	291.0	264.8	63.7	5.5	Welded tuff
GE-4	4	347.0	-9.2	347.0	-9.2	8.3	123.5	268.6	73.3	8.4	Basaltic flow
GE-5[a]	8	291.4	-39.3	291.4	-39.3	3.3	276.1	281.8	17.3	3.9	Basaltic flow
GE-7	8	10.8	-29.6	10.8	-29.6	4.0	232.1	191.3	65.7	4.4	Basaltic flow
GE-8	7	346.8	-21.1	346.8	-21.1	4.6	175.7	255.1	68.6	4.8	Basaltic flow
GER-3	4	351.6	-20.7	351.6	-20.7	6.4	204.3	357.8	80.0	13.1	Basaltic flow
KE-1	8	349.4	-13.1	349.4	-13.1	7.1	73.6	257.2	73.5	7.2	Basaltic flow
KE-2	4	347.3	-21.9	347.3	-21.9	10.9	52.9	253.2	68.5	11.5	Basaltic flow
KE-3	7	8.3	-15.3	8.3	-15.3	11.1	30.6	186.2	73.9	11.4	Basaltic flow
KE-4[b]	4	157.7	39.6	157.7	39.6	23.2	16.6				Basaltic flow
KE-5	5	7.9	-23.9	7.9	-23.9	10.3	57.0	194.3	69.9	11	Basaltic flow
KE-6	4	348.9	-20.7	348.9	-20.7	4.7	386.8	250.7	69.9	4.9	Basaltic flow
KE-7	5	349.0	-18.2	349.0	-18.2	11.1	70.0	252.8	71.1	11.5	Basaltic flow
KE-8	7	348.1	-17.0	348.1	-17.0	5.1	140.0	256.2	71.1	5.3	Basaltic flow
GD-3[a]	5	304.7	8.8	304.7	8.8	3.7	455.0	334.0	79.9	7.0	Basaltic flow
KO-4	5	348.6	16.3	348.6	16.3	10.3	80.6	323.0	78.3	10.6	Basaltic flow
MEK-1	7	349.4	-18.9	349.4	-18.9	5.8	109.8	251.2	71.0	6	Basaltic flow
MEK-2	4	347.5	-20.2	347.5	-20.2	9.0	119.1	254.3	69.3	9.4	Basaltic flow
Mean_N	16	353.5	-16.5	353.6	-16.5	6.0	38.2				
Mean_R	2	161.7	21.8	160.6	19.6	35.8	50.6				
Overall mean[c]	18	352.6	-17	352.6	-17.0	5.5	40.3	243.5	73.5	4.4	

Site name; N, number of samples used to estimate site mean direction; Dg, Ig, Ds and Is, declination and inclination are in situ (g) and tilt-corrected (s); α_{95}, 95% confidence interval; K, precision parameter; ϕs and λs, VGP longitude and latitude, respectively; [a]Transitional directions; [b]sites with α95>15°; [c]An overall mean direction calculated after excluding sites[a and b].

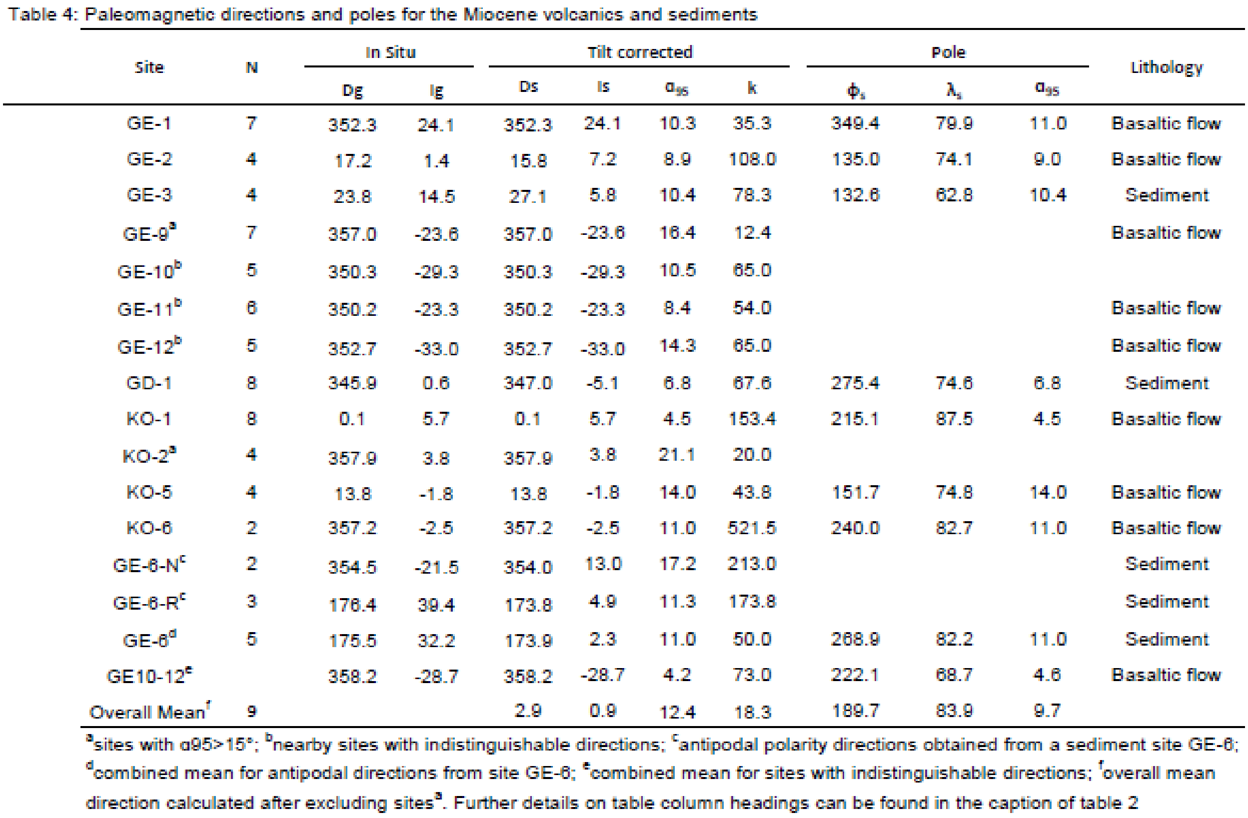

Table 4: Paleomagnetic directions and poles for the Miocene volcanics and sediments

Site	N	In Situ		Tilt corrected				Pole			Lithology
		Dg	Ig	Ds	Is	α_{95}	k	ϕ_s	λ_s	α_{95}	
GE-1	7	352.3	24.1	352.3	24.1	10.3	35.3	349.4	79.9	11.0	Basaltic flow
GE-2	4	17.2	1.4	15.8	7.2	8.9	108.0	135.0	74.1	9.0	Basaltic flow
GE-3	4	23.8	14.5	27.1	5.8	10.4	78.3	132.6	62.8	10.4	Sediment
GE-9[a]	7	357.0	-23.6	357.0	-23.6	16.4	12.4				Basaltic flow
GE-10[b]	5	350.3	-29.3	350.3	-29.3	10.5	65.0				
GE-11[b]	6	350.2	-23.3	350.2	-23.3	8.4	54.0				Basaltic flow
GE-12[b]	5	352.7	-33.0	352.7	-33.0	14.3	65.0				Basaltic flow
GD-1	8	345.9	0.6	347.0	-5.1	6.8	67.6	275.4	74.6	6.8	Sediment
KO-1	8	0.1	5.7	0.1	5.7	4.5	153.4	215.1	87.5	4.5	Basaltic flow
KO-2[a]	4	357.9	3.8	357.9	3.8	21.1	20.0				
KO-5	4	13.8	-1.8	13.8	-1.8	14.0	43.8	151.7	74.8	14.0	Basaltic flow
KO-6	2	357.2	-2.5	357.2	-2.5	11.0	521.5	240.0	82.7	11.0	Basaltic flow
GE-6-N[c]	2	354.5	-21.5	354.0	13.0	17.2	213.0				Sediment
GE-6-R[c]	3	176.4	39.4	173.8	4.9	11.3	173.8				Sediment
GE-6[d]	5	175.5	32.2	173.9	2.3	11.0	50.0	268.9	82.2	11.0	Sediment
GE10-12[e]		358.2	-28.7	358.2	-28.7	4.2	73.0	222.1	68.7	4.6	Basaltic flow
Overall Mean[f]	9			2.9	0.9	12.4	18.3	189.7	83.9	9.7	

[a] sites with α95>15°; [b] nearby sites with indistinguishable directions; [c] antipodal polarity directions obtained from a sediment site GE-6; [d] combined mean for antipodal directions from site GE-6; [e] combined mean for sites with indistinguishable directions; [f] overall mean direction calculated after excluding sites[a]. Further details on table column headings can be found in the caption of table 2

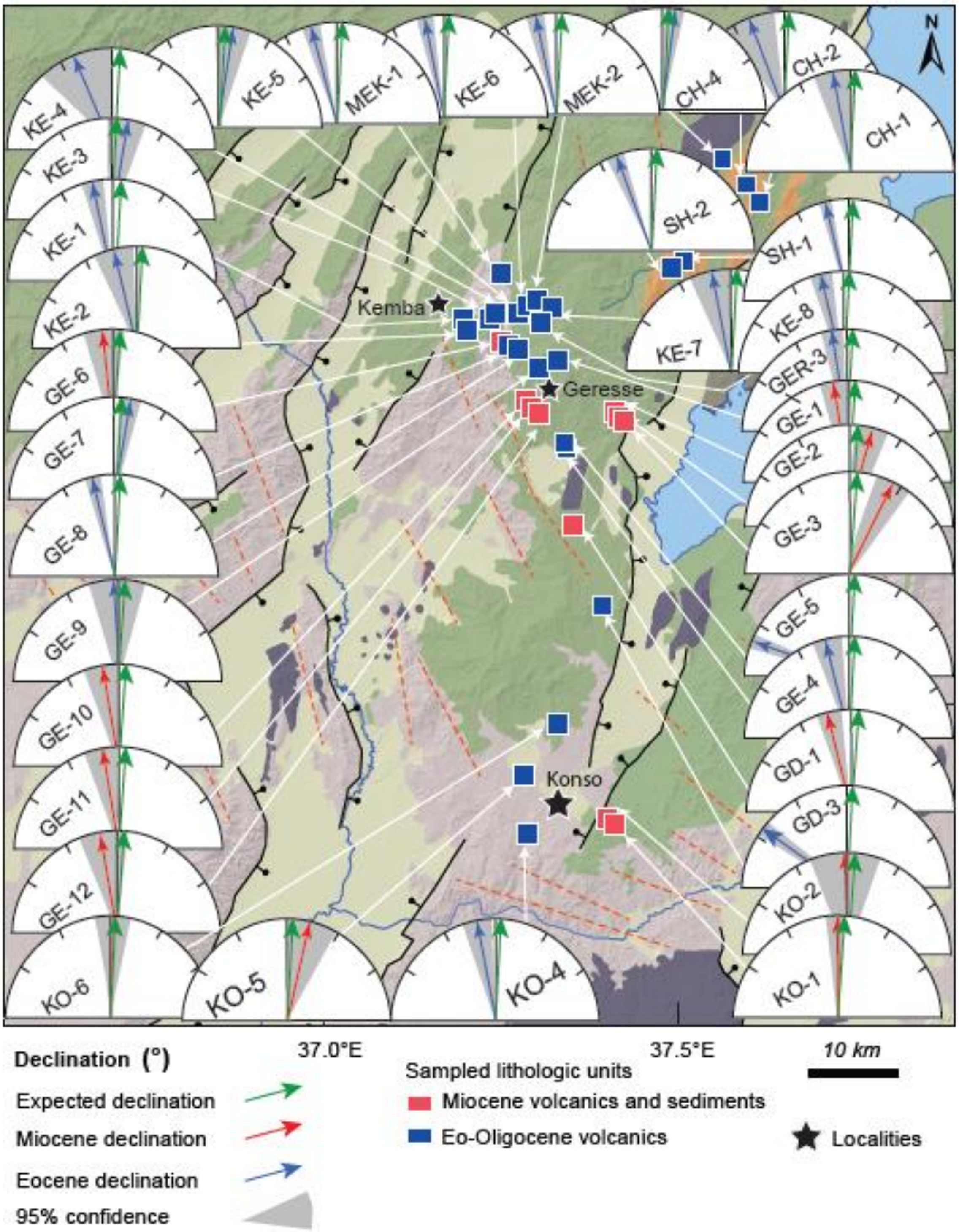

Figure 10: Mean paleomagnetic directions (declination) for each site distributed along and across the Gidole-Chencha Horst superimposed on the sampled stratigraphic units (Davidson, 1983; Bonini et al., 2005) and hill-shaded relief. Squares indicate sampling-site locations of Miocene (red) and Eo–Oligocene (blue) rocks. At each site, the observed mean declination (arrow) is indicated with corresponding 95% confidence interval (gray shaded cone) for the

Eo–Oligocene (dark blue) and Miocene (red) rocks. The green arrows indicate the expected direction relative to the pole for Africa at 40 Ma and 20 Ma for sites of Eo–Oligocene and Miocene ages, respectively.

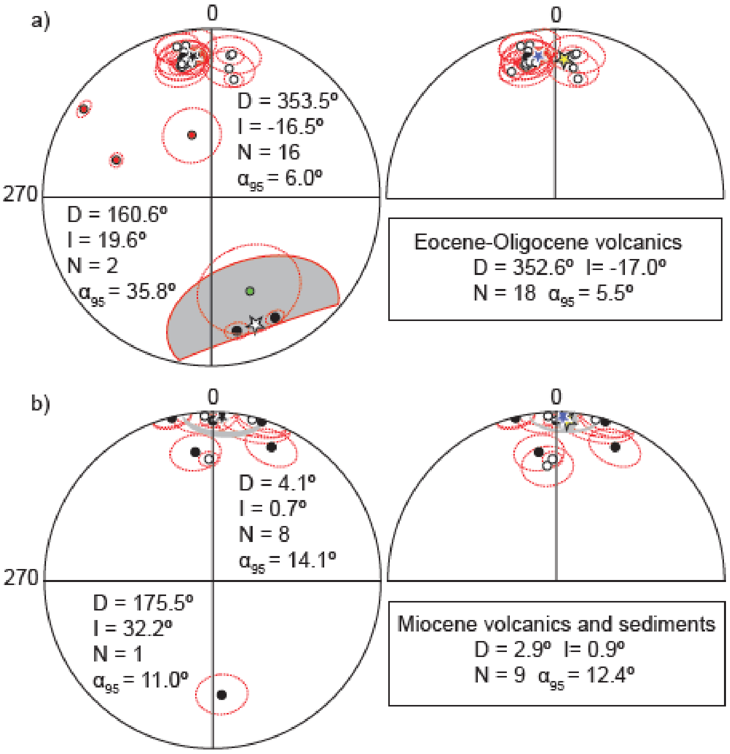

Figure 11. Stereographic projections of individual site mean direction (circle) with 95% confidence interval (red ellipses). Open (full) symbols are projections on the lower (upper) hemisphere. (a) Eo–Oligocene and (b) Miocene rocks. The black, white, blue and yellow stars in the stereographic projections indicate the mean for normal, reversed, overall mean, and expected directions with the corresponding 95% confidence interval (gray circle or envelope). Excluded site mean directions are shown in full red circles for transitional directions and full green circles for directions recording α_{95}>15.

4 Discussion

4.1 Vertical-axis tectonic rotations

To interpret the paleomagnetic data from the Eo–Oligocene and Miocene rocks with respect to the tectonic motion of crustal blocks, the obtained directions must be assessed relative to the African reference plate. In our case, the African APWP for the 10 Myr age windows at 40

Ma (45–35 Ma; Φ_s=191.6°, λ_s=77.3°, α_{95}=7.2°, N=8) and the 5 Myr age window at 20 Ma (15–20 Ma; Φ_s=165.7°, λ_s=81.7°, α_{95}=4.5°, N=16) provided by Besse and Courtillot (2002) are well suited for our Eo–Oligocene and Miocene groups, respectively. Because of the limited motion of African plate, these (Tauxe, 2005) yield expected inclinations for the studied region nearly indistinguishable for the 40 Ma (Φ_s=172.4°, λ_s=84.3°, α_{95}=3.3°, N=24) and 20 Ma (Φ_s=151.9°, λ_s=85.4°, α_{95}=2.7°, N=38) poles, respectively.

A comparison of the observed declination results in map view with the expected declination from the African reference plate (Fig. 10) indicates that the directions of the declinations are not concentrated at a single location; rather, there appear to be small but significant counterclockwise deflections at most Eo–Oligocene sites, reflecting a systematic mechanism that affects the study region. No such trend can be detected at the Miocene sites, which show small variable deflections from the either clockwise or counterclockwise declination expected for the natural dispersion due to the geomagnetic secular variation recorded at those sites.

To assess whether the region was affected by statistically significant vertical-axis rotations, the mean paleomagnetic poles (Fig. 11) are compared with the corresponding reference pole. This yielded a significant counterclockwise rotation (13.2° ± 5.9°) of the mean paleomagnetic pole for the Eo–Oligocene sites relative to the 40 Ma and 20 Ma reference poles, respectively (Besse and Courtillot, 1991, 2002), and no significant systematic vertical-axis rotation (3.7° ± 9.3°) for the Miocene sites. We furthermore used the recently developed procedure described in Vaes et al. (2022), available at *www.APWPonline.org*. This procedure, which is based on an improved statistical approach and database, especially with regard to the age of reference poles (see Vaes et al., 2022 for details), generates a reference VGP that is as close as possible to the age of the studied site. The VGP comparison for the Eo–Oligocene sites relative to the paleopoles for stable Africa in the time range between 35 and 45 Ma results in a significant counterclockwise rotation of R= 11.1°± 6.4° (Fig. 12a). For the Miocene sites, the observed VGPs in the 11–20 Ma age range relative to the pole for Africa results in a statistically insignificant vertical-axis rotation (R = 3.2° ± 11.5°; Fig. 12a). The procedure also yields paleolatitudes that are statistically indistinguishable from those expected for Africa at this location during these times (latitudinal displacements L = 2.8° ± 11.5° and L = 4.2° ± 6.2°, respectively, Fig. 12b). These results are averaged over the region and include dispersion from both geomagnetic secular variation and block rotations. The rotations at the Eo–Oligocene sites appear systematic and strong enough to be detected despite the secular variations. However, this is not the case regarding the Miocene sites, recording no statistically significant rotations based on a more limited number of sites. In that case the large 95° confidence interval does not allow us to discard the hypothesis that some smaller (ca. 10°) rotations did not affect the analyzed sites systematically. More data would be required to determine with greater certainty the difference between the age groups or different sub-regions. Nevertheless, with the available data and a careful review of the regional tectonic events first-order interpretations can be derived.

While it is clear that the age of the rotations postdates the emplacement of the Eocene volcanics between 35 and 45 Ma, further ages constraining the rotations are not straightforward. The similarity and regional distribution of the rotations suggest a common underlying mechanism, although we cannot rule out the possibility that the rotations occurred in several phases at different times and locations. The smaller, and statistically insignificant, rotation documented in the Miocene data set (11–20 Ma) indicates that for the most part the rotations recorded by the Eocene volcanics occurred before the emplacement of the Miocene rocks. In light of these observations, we propose two end-member interpretations: either (1) most of the rotation had already occurred by the Miocene, or (2) the rotations have continued continuously until recently. Below, we discuss the potential implication of the vertical-axis rotations with regard to the regional structural setting and models of rift evolution.

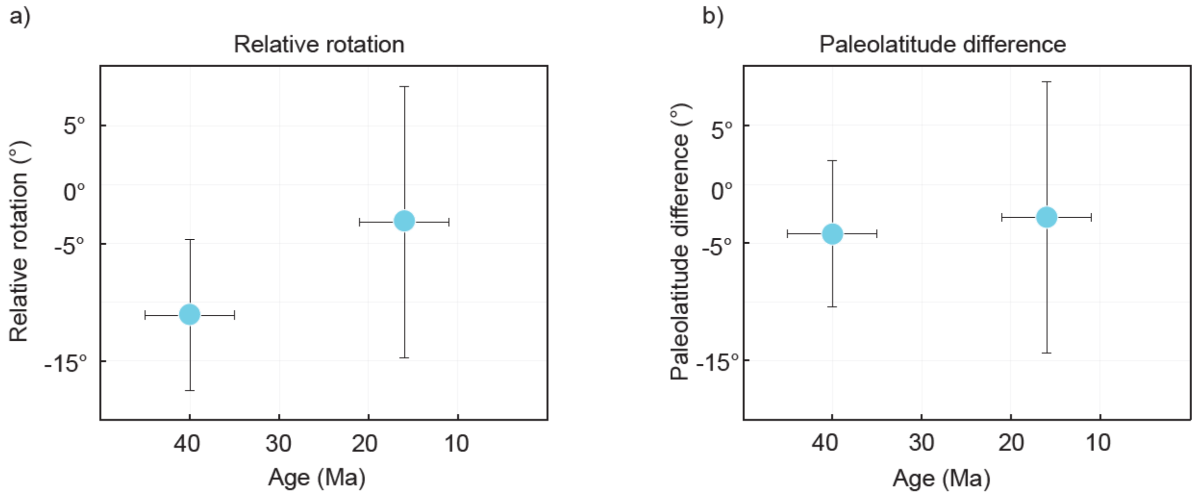

Figure 12. Relative rotation (a) and flattening or latitudinal displacement (b) obtained from comparing the observed Eo–Oligocene and Miocene directions to a reference pole for stable South Africa at a corresponding age range between 35 and 45 Ma (a), and between 11 and 20 Ma (b) (Vaes et al., 2022, 2024).

4.2 Implications for deformation mechanisms

Detected counterclockwise block rotations are consistent with proposed models for the evolution of the southern Main Ethiopian Rift. For example, our results support the expected vertical-axis block rotations that have been suggested in relation to rift overlap between the Chew Bahir Basin-Gofa Province and the southern Main Ethiopian Rift (e.g., Philippon et al., 2014; Brune et al., 2017). Furthermore, the counterclockwise block rotations identified by our analysis support the block-deformation patterns predicted and obtained in analog and numerical modeling studies (Brune et al., 2017; Glerum et al., 2020; Neuharth et al., 2021). Additional insight into the deformation mechanisms can be gained by considering the spatial and temporal characteristics of the extent of vertical-axis block rotation across the overlap zone. By combining our findings with published geologic information from the BRZ, we can further explore and differentiate the temporal variation in the extent of block rotation through two different end-member interpretations of the paleomagnetic data. Our first scenario, which explains the observed vertical-axis rotations by deformation accompanied by counterclockwise block rotation starting between 27 and 20 Ma, synchronous with faulting (e.g., Pik et al., 2008; Erbello et al., 2024), and continuing until the present day. In this model of sustained rotation and deformation, the Eo–Oligocene volcanics would thus record a larger amount of tectonic overprint than the Miocene volcanic and sedimentary sequences. In the second scenario, much of the vertical-axis block rotation would have occurred during the initial rifting phase between 27 and 20 Ma and would have affected the Eo–Oligocene volcanics; however, in this case the region would have only experienced limited block rotations since the late Miocene.

This second scenario appears to be more consistent with the regional spatial change in tectonic activity during the Mio–Pliocene (e.g., Davidson, 1983, Ebinger et al., 2000; Chorowicz, 2005; WoldeGabriel et al., 1991; Ebinger et al., 1993, 2000; Bonini et al., 2005; Pik et al., 2008; Philippon et al., 2014, Brune et al., 2017; Boone et al., 2019; Corti et al., 2019; Erbello et al., 2024). Geochronologic, structural, and field data from the southern Main Ethiopian Rift indicate that major faulting along the eastern margin of the Gidole-Chencha Horst occurred between 18 and 14 Ma (Ebinger et al., 2000). Following the development of the marginal fault, deformation migrated toward the Segen Basin and a narrow zone of the southern Main Ethiopian Rift during the middle Miocene and Pliocene, respectively (Levitte, 1974; WoldeGabriel et al., 1991; Ebinger et al., 2000; Bonini et al., 2005). West of the Gidole-Chencha Horst along the Gofa Province, a concurrent shift in deformation toward the southern Gofa Province and the Chew Bahir Basin was suggested by WoldeGabriel et al. (1991) and Ebinger et al. (2000). Recent geomorphic investigation of river catchments verified by field observations along the western margin of the Mali-Dancha and Bala-Kela areas in the Gofa Province reveal Quaternary normal faults and young tectonic landforms, suggesting strain localization along a narrow zone in the Gofa Province (Erbello et al., 2022; 2024). The documented spatiotemporal variation in tectonic activity across the BRZ (Philippon et al., 2014; Erbello et al., 2022; 2024) is therefore consistent with the second scenario discussed above. A significant amount of counterclockwise block rotation would have occurred during the early Miocene, mainly prior to the deposition of the Miocene volcanics and sediments, which was superseded by a decrease in block rotation and accompanied by strain localization in the current rift sectors.

Finally, our interpretation that rotation ceased in the middle Miocene is consistent with geodetic observations, indicating insignificant present-day block rotation (Knappe et al., 2020). We note, however, that in the first scenario, the observed rotation of 11.1°± 6.4° that has been distributed continuously since 20 Ma, would imply a rotation of ca. 0.5°/Myr, an amount difficult to detect with GPS surveys over such a small region and only spanning a few years or decades. In future studies, a detailed comparison between paleomagnetic data and geodetic observations may lead to more reliable assessments of current deformation patterns involving vertical axis rotations. However, such a comparison would require high-resolution paleomagnetic sampling of Miocene–Holocene volcano-stratigraphic units over an extensive region and a GPS network with sufficient spatial and temporal coverage to detect such small signals.

4.3 The role of inherited lineaments in extensional tectonics

In light of the spatiotemporal changes of the locations of volcanism and extension in southern Ethiopia (e.g., Ebinger et al., 2000, Philippon et al., 2014, Corti et al., 2019, Knappe et al., 2020), it is expected that the degree to which tectonic processes reactivated inherited crustal-scale heterogeneities during the Cenozoic has also changed over time. In such a scenario, where vertical-axis rotations involve structural blocks with a diffuse shearing of pre-existing fabrics inherited from previous geodynamic processes (Erbello et al., 2024), it can be inferred that the NW-SE-striking inherited zones of weakness parallel to the rotating blocks may have facilitated lateral motion and efficient kinematic transfer between different rift sectors. For example, the counterclockwise block rotation of ~11 ± 6.4° recorded from the Eo–Oligocene volcanic rocks appears to have decreased significantly over time, as documented by the paleomagnetic signals obtained from the Miocene volcanics. The large extent of vertical axis block rotation might have been facilitated by regional diffuse shear along the NW-SE-oriented lineaments achieved during early rifting (Boone et al., 2019; Erbello et al., 2024;). However, due to the overall block motion, this process would have later slowed down as the overlapping rift segments would have connected to develop larger, throughgoing extensional structures (e.g., Neuharth et al., 2021). In this context, it is noteworthy that low-temperature thermochronologic data from the Gofa Province record rapid exhumation across the NW-SE-oriented the Beto and Mali-Dancha basin margins during the early Miocene (Boone et al., 2019; Erbello et al., 2024). The reactivation of the NW-SE-striking lineaments during the early Miocene thus likely reflects the role of inherited zones of weakness in facilitating fracture propagation during the initial rifting processes (Fig. 13).

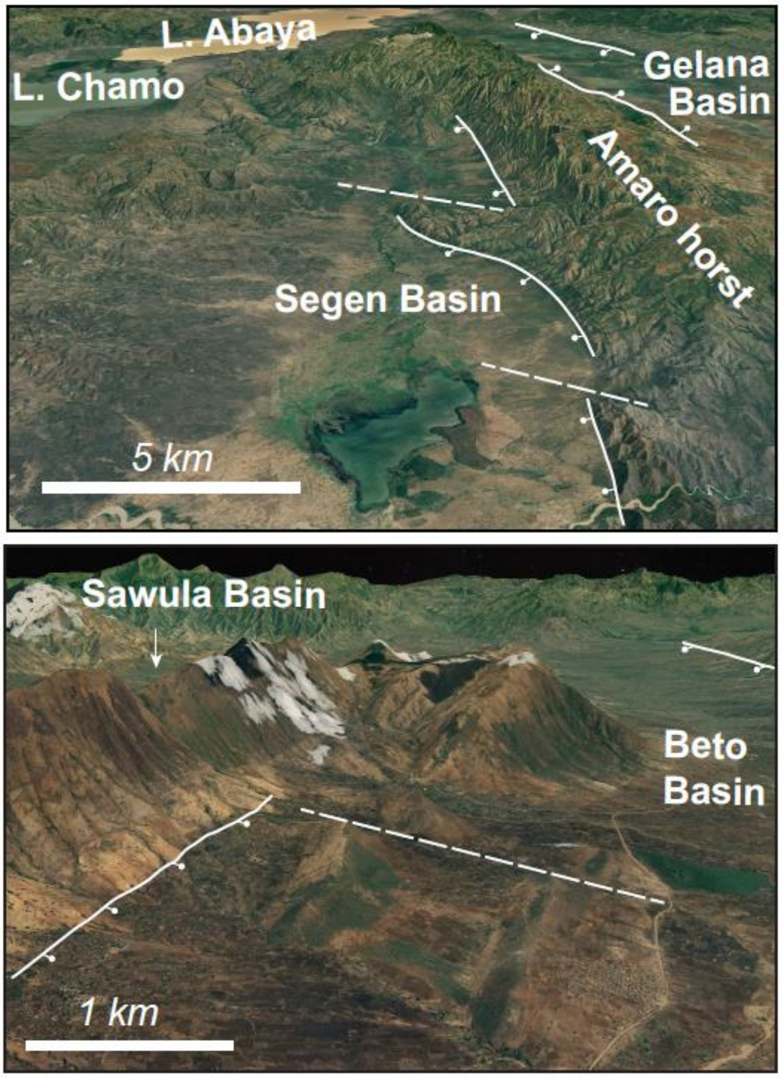

Figure 13. Northwest-view of the southern Main Ethiopian Rift (Segen, Chamo, Gelana, and Abaya basins) and the Gofa Province (Beto and Sawula basins) with basin-bounding faults

(white extended lines with ball and bar symbol). The satellite image is from © Google Earth. The white broken lines indicate NW-SE-striking lineaments with an inferred strike-slip component.

In the context of pre-existing crustal heterogeneities that may facilitate fracture propagation, it is interesting that recent seismic tomographic imaging from the BRZ reveals a near-vertical, NW-SE-trending pervasive band of lineaments below the southern Gofa Province and the northern Chew Bahir Basin (Kounoudis et al., 2021). Additionally, thermochronologic data from this region, obtained at the margin of the Gofa Province, show spatial variations in the onset of faulting and tectonic exhumation (e.g., Balestrieri et al., 2016). Lineaments striking at high angles with respect to the orientation of the rift (Fig. 13), such as the NW-SE-striking reactivated Mesozoic rift-related structures in the BRZ (Bosworth, 1992), may have inhibited meridionally oriented fault propagation and accommodated extensional processes by shearing along these inherited anisotropies (e.g., Molnar et al., 2019).

In line with these observations are earthquake focal mechanism solutions and geological observations that partly indicate a component of horizontal shearing and oblique normal faulting within this Ethiopian extensional province. For example, Asfaw (1990) identified Quaternary oblique-slip faulting along the basin-bounding Chew Bahir and southern Gofa Province faults. Furthermore, earthquakes recorded in the Chew Bahir Basin, the Segen Basin, and more distant regions in the northwestern sector of South Sudan, suggest strike-slip faulting along the NW-SE- and N-S-striking lineaments (Ayele, 2000 and Arvidsson). Finally, a seismicity study in the BRZ and the northern Kenya Rift revealed right-lateral strike-slip faulting in the transition between the southern Main Ethiopian and northern Kenya rifts (Musila et al., 2023; Sullivan et al., 2024). This is consistent with the reactivation of NW-SE-striking lineaments similar to structures depicted in Figures 13 and 14 of our study. The existence of such structures may have facilitated the counterclockwise block rotation between both rift sectors, although lateral displacement along the lineaments appears to have been limited (Fig. 13) (Ebinger et al., 2000).

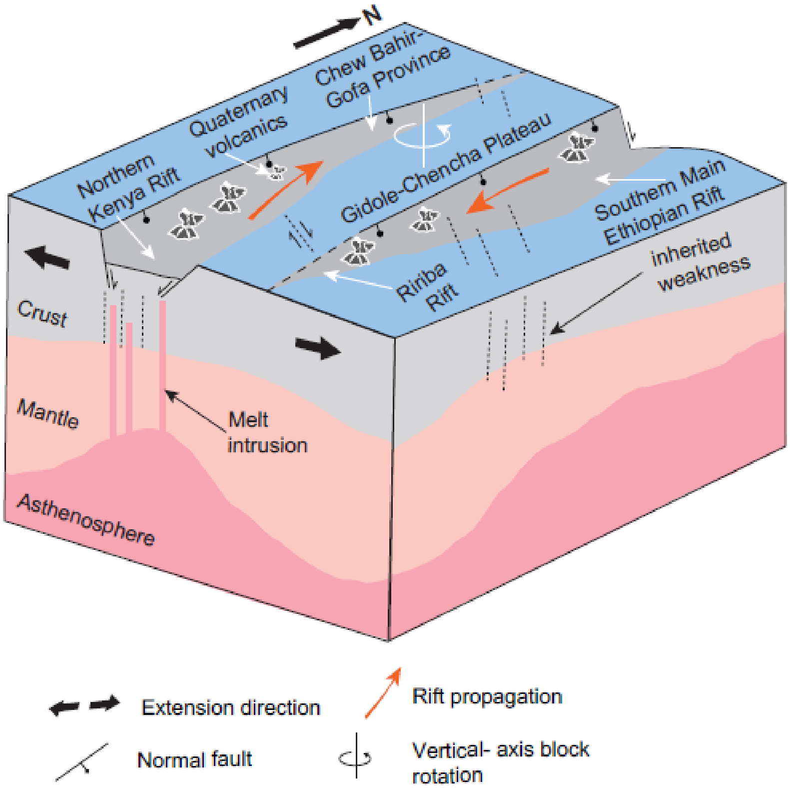

Figure 14. Oppositely propagating, parallel rift segments and associated vertical axis block rotation across the overlap zone between the southern Main Ethiopian Rift and the Chew Bahir Basin-Gofa Province. The black and orange arrows indicate local plate kinematics (Philippon et al., 2014) and direction of propagating rift segments, respectively. Inferred NW-SE-striking inherited crustal-scale lineaments shown as gray broken lines. The regional-scale model depicting lithospheric structure associated with magmatic intrusions is modified from Ebinger et al. (2000) and Corti (2009).

5 Conclusions

Paleomagnetic data combined with published and new ^{40}Ar/^{39}Ar data from the ~40-km-wide zone of overlap between the bi-directionally propagating southern Main Ethiopian Rift and the Chew Bahir Basin-Gofa extensional Province reveal a temporal evolution of deformation associated with post–Eocene, approximately 10 to 15° counterclockwise regional vertical-axis block rotations.

The combined data set suggests a decrease in the amount of vertical-axis block rotation through time that corresponds well with the migration of deformation toward the axial zone of the southern Main Ethiopian Rift and the extensional Chew Bahir Basin-Gofa Province. In light of regional structural and low-temperature thermochronology data our observations suggest that much of the deformation related to the vertical-axis block rotations likely occurred in the early Miocene, approximately starting between 18 and 14 Ma and progressively decreasing subsequently to a migration of the locus of deformation toward the rift axis during the Pliocene.

The pattern of regional counterclockwise block rotations that most likely occurred during early Miocene initial rifting, is inferred to be related to the reactivation of NW-SE-striking Mesozoic lineaments, reflecting the influence of inherited structures on the propagation of fractures and faults during extension. However, further paleomagnetic studies are necessary to ascertain the timing of rotations. The rich volcanic record of southern Ethiopia would provide the opportunity to do this in rare detail. Our study demonstrates the potential of paleomagnetic analyses to constrain tectonic models and quantitatively define the extent of extensional deformation of southern Ethiopia.

Acknowledgments

This research was funded by the DAAD through a grant to A. Erbello (German Academic Exchange Service). Additional support came from the Geothermal Development Company, Kenya and funds provided by the Faculty of Mathematics and Natural Sciences of the University of Potsdam to M. Strecker. D. Melnick was funded by the German Research Foundation (DFG), grant ME-3157/4-2. We thank Asfawossen Asrat for having provided us with paleomagnetic sampling equipment. We thank the government offices of Gamo and Gofa for administrative and logistic support. Finally, we would like to thank Ermias Filfilu and Ameha Atnafu Muluneh for their support and H. Pingel for suggestions to improve the illustrations.

Authorship contribution statement

A. Erbello: Writing – review & editing, Writing – original draft, Visualization, Software,

Methodology, Investigation, Formal analysis, Data curation, Conceptualization.

G. Dupont-Nivet: Writing – review & editing, Validation, Supervision, Methodology, Investigation, Formal analysis, Conceptualization.

M. R. Strecker: Writing – review & editing, Validation, Supervision, Methodology, Investigation, Formal analysis, Conceptualization.

T. Kidane: Writing – review & editing, Validation, Methodology, Conceptualization.

N. Nowaczyk: Writing – review & editing, Validation, Software, Data curation.

M. Sudo: Writing – review & editing, Validation, Software, Methodology, Data curation.

D. Melnick: Writing – review & editing, Validation, Supervision, Conceptualization.

B. Bookhagen: Writing – review & editing, Visualization, Validation, Supervision, Conceptualization.

S. Brune: Writing – review & editing, Validation, Conceptualization.

G. Corti: Writing – review & editing, Validation, Conceptualization.

G. Gecho: Writing – review & editing, Validation.

Data availability

All the data supporting this research are available in the text and supplementary materials. The supplementary materials can be found at https://doi.org/ 10.5281/zenodo.12247088. Additional data can be found upon request to the corresponding author.

6 References

Aanyu, K., and Koehn, D. (2011), Influence of pre-existing fabrics on fault kinematics and rift geometry of interacting segments: Analogue models based on the Albertine Rift (Uganda), Western Branch-East African Rift System. Journal of African Earth Sciences. doi:10.1016/j.jafrearsci.2010.10.003

Acocella, V., Morvillo, P., and Funiciello, R. (2005), What controls relay ramps and transfer faults within rift zones? Insights from analogue models. Journal of Structural Geology. doi:10.1016/j.jsg.2004.11.006

Acton, G.D., Stein, S., and Engeln, J.F. (1991), Block rotation and continental extension in Afar: A comparison to oceanic microplate systems. Tectonics, doi:10.1029/90TC01792

Asfaw, L.M. (1990), Implication of shear deformation and earthquake distribution in the East African Rift between 4°N and 6°N. Journal of African Earth Sciences. doi:10.1016/0899-5362(90)90041-C

Ayele, A., and Arvidsson, R. (1997), Fault mechanisms and tectonic implication of the 1985-1987 earthquake sequence in south-western Ethiopia. Journal of Seismology. doi:10.1023/A:1009774331917

Balestrieri, M.L., Bonini, M., Corti, G., Sani, F., and Philippon, M. (2016), A refinement of the chronology of rift-related faulting in the Broadly Rifted Zone, southern Ethiopia, through apatite fission-track analysis. Tectonophysics, 671, 42–55. doi:10.1016/j.tecto.2016.01.012

Bellahsen, N., Leroy, S., Autin, J., Razin, P., d'Acremont, E., Sloan, H., Pik, R., Ahmed, A., and Khanbari, K. (2013), Pre-existing oblique transfer zones and transfer/transform relationships in continental margins: New insights from the southeastern Gulf of Aden, Socotra Island, Yemen. Tectonophysics. doi:10.1016/j.tecto.2013.07.036

Besse, J., and Courtillot, V. (2002), Apparent and true polar wander and the geometry of the geomagnetic field over the last 200 Myr. Journal of Geophysical Research: Solid Earth. doi:10.1029/2000jb000050

Besse, J., and Courtillot, V. (1991), Revised and synthetic apparent polar wander paths of the African, Eurasian, North American and Indian plates, and true polar wander since 200 Ma. Journal of Geophysical Research. doi:10.1029/90JB01916

Bonini, M., Corti, G., Innocenti, F., Manetti, P., Mazzarini, F., Abebe, T., and Pecskay, Z. (2005), Evolution of the Main Ethiopian Rift in the frame of Afar and Kenya rifts propagation. Tectonics. doi:10.1029/2004TC001680

Boone, S. C., Balestrieri, M.L., Kohn, B.P., Corti, G., Gleadow, A.J.W., and Seiler, C. (2019), Tectonothermal Evolution of the Broadly Rifted Zone, Ethiopian Rift. Tectonics. doi:10.1029/2018TC005210

Boone, Samuel C., Kohn, B.P., Gleadow, A.J.W., Morley, C.K., Seiler, C., Foster, D.A. (2019), Birth of the East African Rift System: Nucleation of magmatism and strain in the Turkana Depression. Geology. doi:10.1130/G46468.1

Bosworth, W. (1992), Mesozoic and Early Tertiary rift tectonics in East Africa. Tectonophysics. doi:10.1016/0040-1951(92)90014-W

Bosworth, W. (1985), Geometry of propagating continental rifts. Nature. doi:10.1038/316625a0

Bosworth, W., and Morley, C.K. (1994), Structural and stratigraphic evolution of the Anza rift, Kenya. Tectonophysics. doi:10.1016/0040-1951(94)90171-6

Brune, S., Corti, G., and Ranalli, G. (2017), Controls of inherited lithospheric heterogeneity on rift linkage: Numerical and analog models of interaction between the Kenyan and Ethiopian rifts across the Turkana depression. Tectonics. doi:10.1002/2017TC004739

Butler, R.F., 1992. Paleomagnetism: Magnetic Domains to Geologic Terranes. Blackwell, Boston, MA, 319 p.

Childs, C., Easton, S.J., Vendeville, B.C., Jackson, M.P.A., Lin, S.T., Walsh, J.J., and Watterson, J. (1993), Kinematic analysis of faults in a physical model of growth faulting above a viscous salt analogue. Tectonophysics. doi:10.1016/0040-1951(93)90346-L

Childs, C., Watterson, J., and Walsh, J.J. (1995), Fault overlap zones within developing normal fault systems. Journal of the Geological Society of London. doi:10.1144/gsjgs.152.3.0535

Chorowicz, J. (2005), The East African rift system. Journal of African Earth Sciences. doi:10.1016/j.jafrearsci.2005.07.019

Chu, D., and Gordon, R.G. (1999), Evidence for motion between Nubia and Somalia along the Southwest Indian Ridge. Nature. doi:10.1038/18014

Cogne, J.P. (2003), PaleoMac: A Macintosh^{TM} application for treating paleomagnetic data and making plate reconstructions. Geochemstry, Geophysics, Geoszstems, 4(1), 1-8. doi:10.1029/2001GC000227, 2003.

Corti, G. (2008), Control of rift obliquity on the evolution and segmentation of the Main Ethiopian Rift. Nature Geoscience. doi:10.1038/ngeo160

Corti, G., Cioni, R., Franceschini, Z., Sani, F., Scaillet, S., Molin, P., Isola, I., Mazzarini, F., Brune, S., Keir, D., Erbello, A., Muluneh, A., Illsley-Kemp, F., and Glerum, A. (2019), Aborted propagation of the Ethiopian rift caused by linkage with the Kenyan rift. Nature Communications, 10. doi:10.1038/s41467-019-09335-2

Cox, A. (1973), Tectonics and Geomagnetic Reversals. W.H. Freeman, San Francisco, CA, p. 702 p

Dawers, N.H., and Anders, M.H. (1995), Displacement-length scaling and fault linkage. Journal of Structural Geology. doi:10.1016/0191-8141(94)00091-D

Deenen, M.H., Langereis, C.G., van Hinsbergen, D.J., and Biggin, A.J. (2011), Geomagnetic secular variation and the statistics of paleomagnetic directions. Geophysical Journal International doi:10.1111/j.1365-246X.2011.05050.x

DeMets, C., Merkouriev, S., and Sauter, D. (2015), High-resolution estimates of Southwest Indian Ridge plate motions, 20 Ma to present. Geophysical Journal International. doi:10.1093/gji/ggv366

Dommain, R., Riedl, S., Olaka, L.A., DeMenocal, P., Deino, A.L., Owen, R.B., Muiruri, V., Müller, J., Potts, R., and Strecker, M.R. (2022), Holocene bidirectional river system along the Kenya Rift and its influence on East African faunal exchange and diversity gradients. Proceedings of the National Academy of Sciences 119. doi:10.1073/pnas.2121388119

Dunlop, D.J., Özdemir, O. (1997), Rock Magnetism: Fundamentals and Frontiers. Cambridge University Press, Cambridge 573 p.

Ebinger, C., and Scholz, C.A. (2012), Continental Rift Basins: The East African Perspective. in: Busby, C., Azor, A. (Eds.), Tectonics of Sedimentary Basins: Recent Advances. doi:10.1002/9781444347166.ch9

Ebinger, C.J., Jackson, J.A., Foster, A.N., and Hayward, N.J. (1999), Extensional basin geometry and the elastic lithosphere. Philosophical Transactions of the Royal Society A: Mathematical, Physical and Engineering Sciences. doi:10.1098/rsta.1999.0351

Ebinger, C.J., Yemane, T., Harding, D.J., Tesfaye, S., Kelley, S., and Rex, D.C. (2000), Rift deflection, migration, and propagation: Linkage of the Ethiopian and Eastern rifts, Africa.

Bulletin of the Geological Society of America. doi:10.1130/0016-7606(2000)112<163:RDMAPL>2.0.CO;2

Ebinger, C.J., Yemane, T., Woldegabriel, G., Aronson, J.L., and Walter, R.C. (1993), Late Ecocene-Recent volcanism and faulting in the southern main Ethiopian rift. Journal of the Geological Society of London. doi:10.1144/gsjgs.150.1.0099

Emishaw, L., and Abdelsalam, M.G. (2019), Development of Late Jurassic-Early Paleogene and Neogene-Quaternary rifts within the Turkana Depression, East Africa from satellite gravity data. Tectonics, 38, 2358–2377. doi:10.1029/2018TC005389

Erbello, A., and Kidane, T. (2018), Timing of volcanism and initiation of rifting in the Omo-Turkana depression, southwest Ethiopia: Evidence from paleomagnetism. Journal of African Earth Sciences. doi:10.1016/j.jafrearsci.2017.12.031

Erbello, A., Melnick, D., Zeilinger, G., Bookhagen, B., Pingel, H., and Strecker, M.R. (2022), Geomorphic expression of a tectonically active rift-transfer zone in southern Ethiopia. Geomorphology. doi:10.1016/j.geomorph.2022.108162

Erbello, A., Colleps, C., Melnick, D., Sobel, E.R., Bookhagen, B., Pingel, H., Zeilinger, G., van der Beek, P., and Strecker, M.R. (2024), Magma-assisted continental rifting: The broadly rifted zone of SW Ethiopia, East Africa. Tectonics. doi:10.1029/2022TC007651

Erbello. A., Dupont-Nivet. G., Kidane. T., Nowaczyk. N., Sudo. M., Melnick. D., Bookhagen. B., Brune. S., Corti. G., Gecho. G., and Strecker, M.R. (2023), Temporal variation in counterclockwise vertical-axis block rotations across a rift overlap zone, southwestern Ethiopia, East Africa [data set]. Zenodo. doi: 10.5281/zenodo.8263190

Fernandes, R.M.S., Miranda, J.M., Delvaux, D., Stamps, D.S., and Saria, E. (2013), Re-evaluation of the kinematics of the Victoria block using continuous GNSS data. Geophysical Journal International. doi:10.1093/gji/ggs071

Fisher, R. (1953), Dispersion on a sphere. Proceedings of the Royal Society A: Mathematical, Physical and Engineering Sciences. doi:10.1098/rspa.1953.0064

Faccenna, C., Glišović, P., Forte, A., Becker, T.W., Garzanti, E., Sembroni, A., and Gvirtzman, Z. (2019), Role of dynamic topography in sustaining the Nile River over 30 million years.

Nature Geoscience. doi:10.1038/s41561-019-0472-x

Fleck, R. J., J. F. Sutter and D. H. Elliot (1977): Interpretation of discordant ^{40}Ar/^{39}Ar age-spectra of Mesozoic tholeiites from Antarctica. Geochimica et Cosmochimica Acta, 41, 15-32

Franceschini, Z., Cioni, R., Scaillet, S., Corti, G., Sani, F., Isola, I., Mazzarini, F., Duval, F., Erbello, A., Muluneh, A., and Brune, S. (2020), Recent volcano-tectonic activity of the Ririba rift and the evolution of rifting in South Ethiopia. Journal of Volcanology and Geothermal Research. doi:10.1016/j.jvolgeores.2020.106989

Garcin, Y., Melnick, D., Strecker, M.R., Olago, D., and Tiercelin, J.-J. (2012), East African mid-Holocene wet–dry transition recorded in palaeo-shorelines of Lake Turkana, northern Kenya Holocene wet–dry transition recorded in palaeo-shorelines of Lake Turkana, northern Kenya. Earth Planet. Sci. Lett. 331–332, 322–334. doi.org/ 10.1016/j.epsl.2012.03.016.

Glerum, A., Brune, S., Stamps, D.S., and Strecker, M.R. (2020), Victoria continental microplate dynamics controlled by the lithospheric strength distribution of the East African Rift. Nature Communications. doi:10.1038/s41467-020-16176-x

Gouin, P. (1979), Earthquake History of Ethiopia and the Horn Of Africa. Geophysical Observatory,University of Addis Ababa, Addis Ababa.

Halama, R., M. Konrad-Schmolke, M. Sudo, H. Marschall and M. Wiedenbeck (2014): Effects of fluid-rock interaction on ^{40}Ar/^{39}Ar geochronology in high-pressure rocks (Sesia-Lanzo Zone, Western Alps). Geochimica et Cosmochimica Acta, 126, 475-494

Hetzel, R., and Strecker, M.R. (1994), Late Mozambique Belt structures in western Kenya and their influence on the evolution of the Cenozoic Kenya Rift. Journal of Structural Geology. doi:10.1016/0191-8141(94)90104-X

Johnson, C.L., Constable, C.G., Tauxe, L., Barendegt, R., Brown, L.L., Coe, R.S, and Stone, D.B. (2008), Recent investigations of the 0–5 Ma geomagnetic field recorded by lava flows. Geochemistry, Geophysics, Geosystems. doi:10.1029/2007GC001696

Katz, R.F., Ragnarsson, R., and Bodenschatz, E. (2005), Tectonic microplates in a wax model of sea-floor spreading. New Journal of Physics. doi:10.1088/1367-2630/7/1/037

Kidane, T., Courtillot, V., Manighetti, I., Audin, L., Lahitte, P., Quidelleur, X., Gillot, P.-Y., Gallet, Y., Carlut, J., and Haile, T. (2003), New paleomagnetic and geochronologic results from Ethiopian Afar: Block rotations linked to rift overlap and propagation and determination of a ~2 Ma reference pole for stable Africa. Journal of Geophysical Research: Solid Earth. doi:10.1029/2001jb000645

Kidane, T., Otofuji, Y.I., Komatsu, Y., Shibasaki, H., and Rowland, J. (2009), Paleomagnetism of the Fentale magmatic segment, Main Ethiopian Rift: New evidence for counterclockwise block rotation linked to transtensional deformation. Physics of the Earth and Planetary Interiors. doi:10.1016/j.pepi.2009.04.006

Kirschvink, J.L. (1980), The least-squares line and plane and the analysis of palaeomagnetic data. Geophysical Journal of the Royal Astronomical Society. doi:10.1111/j.1365-246X.1980.tb02601.x

Knappe, E., Bendick, R., Ebinger, C., Birhanu, Y., Lewi, E., Floyd, M., King, R., Kianji, G., Mariita, N., Temtime, T., Waktola, B., Deresse, B., Musila, M., Kanoti, J., and Perry, M. (2020), Accommodation of East African rifting across the Turkana Depression. Journal of Geophysical Research: Solid Earth. doi:10.1029/2019JB018469

Koehn, D., Aanyu, K., Haines, S., and Sachau, T. (2008), Rift nucleation, rift propagation and the creation of basement micro-plates within active rifts. Tectonophysics. doi:10.1016/j.tecto.2007.10.003

Kolawole, F., Firkins, M.C., Al Wahaibi, T.S., Atekwana, E.A., and Soreghan, M.J. (2021), Rift interaction zones and the stages of rift linkage in active segmented continental rift systems. Basin Research 33. doi:10.1111/bre.12592

Koukouvelas, I.K., Asimakopoulos, M., and Doutsos, T.T. (1999), Fractal characteristics of active normal faults: An example of the eastern Gulf of Corinth, Greece. Tectonophysics. doi:10.1016/S0040-1951(99)00087-6

Kounoudis, R., Bastow, I.D., Ebinger, C.J., Ogden, C.S., Ayele, A., Bendick, R., Mariita, N., Kianji, G., Wigham, G., Musila, M., and Kibret, B. (2021), Body-wave tomographic imaging of the Turkana Depression: Implications for rift development and plume-lithosphere interactions. Geochemistry, Geophysics, Geosystems. doi:10.1029/2021GC009782

Lee, J-Y., Marti, K., Severinghaus, J.P., Kawamura, K., Yoo, H-S., Lee, J.B., and Kim, J.S. (2006), A redetermination of the isotopic abundances of atmospheric Ar. Geochimica et Cosmochimica Acta, 70, 4507-4512. doi: 10.1016/j.gca.2006.06.1563

Levitte, D., Columba, J., and Mohr, P. (1974), Reconnaissance geology of the Amaro Horst, southern Ethiopian Rift. Geological Society of America Bulletin. doi:10.1130/0016-7606(1974)85<417:RGOTAH>2.0.CO;2

MacDonald, K.C., and Fox, P.J. (1983), Overlapping spreading centres: New accretion geometry on the East Pacific Rise. Nature. doi:10.1038/302055a0

McKenzie, D., and Jackson, J. (1986), A block model of distributed deformation by faulting. Journal of the Geological Society. doi:10.1144/gsjgs.143.2.0349

Michael Kendall, J., and Lithgow-Bertelloni, C. (2016), Why is Africa rifting?, in: Journal of the Geological Society Special Publication. doi:10.1144/SP420.17

Molnar, N.E., Cruden, A.R., and Betts, P.G. (2019), Interactions between propagating rifts and linear weaknesses in the lower crust. Geosphere. doi:10.1130/GES02119.1

Moore, J.M., and Davidson, A. (1978), Rift structure in southern Ethiopia. Tectonophysics. doi:10.1016/0040-1951(78)90111-7

Morgan, L.E., D.F. Mark, J. Imlach, D. Barfod, R. Dymock (2014): FCs-EK: a new sampling of the Fish Canyon Tuff ^{40}Ar/^{39}Ar neutron flux monitor. Jourdan, F., Mark, D.F. & Verati, C. (eds.) 2014. Advances in ^{40}Ar/^{39}Ar Dating: from Archaeology to Planetary Sciences. Journal of the Geological Society Special Publication, 378, 63-67

Morley, C.K., Nelson, R.A., Patton, T.L., and Munn, S.G. (1990), Transfer zones in the East African Rift System and their relevance to hydrocarbon exploration in rifts. American Association of Petroleum Geologists Bulletin. doi:10.1306/0c9b2475-1710-11d7-8645000102c1865d

Morley, C.K., Wescott, W.A., Stone, D.M., Harper, R.M., Wigger, S.T., and Karanja, F.M.

(1992), Tectonic evolution of the northern Kenyan Rift. Journal of the Geological Society . doi:10.1144/gsjgs.149.3.0333

Muluneh, A.A., Kidane, T., Rowland, J., and Bachtadse, V. (2013), Counterclockwise block rotation linked to southward propagation and overlap of sub-aerial Red Sea Rift segments, Afar Depression: Insight from paleomagnetism. Tectonophysics. doi:10.1016/j.tecto.2013.02.030

Musila, M., C. J. Ebinger, I. D. Bastow, G. Sullivan, S. J. Oliva, E. Knappe, M. Perry, R. Kounoudis, C. S. Ogden, R. Bendick, S. Mwangi, N. Mariita, G. Kianji, E. Klein, F. Illsley-Kemp (2023), Active deformation constraints on the Nubia-Somalia Plate Boundary through Heterogeneous Lithosphere of the Turkana Depression, Geochemistry, Geophysics, Geosystems. doi: 10.1029/2023GC0109822023GC010982

Nelson, R.A., Patton, T.L., and Morley, C.K. (1992), Rift-segment interaction and its relation to hydrocarbon exploration in continental rift systems. American Association of Petroleum Geologists Bulletin. doi:10.1306/bdff898e-1718-11d7-8645000102c1865d

Neuharth, D., Brune, S., Glerum, A., Helne, C., and Welford, J.K. (2021), Formation of continental microplate through rift linkage: numerical modeling and its application to the Flemish Cap and Sao Paulo Plateau. Geochemistry, Geophysics, Geosystems. doi:10.1029/2020GC009615

Nugsse, K., Muluneh, A.A., and Kidane, T. (2018), Paleomagnetic evidence for counterclockwise rotation of the Dofan magmatic segment, Main Ethiopian Rift. Tectonophysics. doi10.1016/j.tecto.2018.03.013

Olaka, L.A., Kasemann, S.A., Sültenfuß, J., Wilke, F.D.H., Olago, D.O., Mulch, A., and Musolff, A. (2022), Tectonic control of groundwater recharge and flow in faulted volcanic aquifers. Water Resources Research. doi:10.1029/2022WR032016

Peacock, D.C.P. (2002), Propagation, interaction and linkage in normal fault systems. Earth-Science Reviews. doi:10.1016/S0012-8252(01)00085-X

Philippon, M., Corti, G., Sani, F., Bonini, M., Balestrieri, M.L., Molin, P., Willingshofer, E., Sokoutis, D., and Cloetingh, S. (2014), Evolution, distribution, and characteristics of rifting in southern Ethiopia. Tectonics. doi:10.1002/2013TC003430

Pik, R., Marty, B., Carignan, J., Yirgu, G., and Ayalew, T. (2008), Timing of East African Rift development in southern Ethiopia: Implication for mantle plume activity and evolution of topography. Geology. doi:10.1130/G24233A.1

Ragon, T., Nutz, A., Schuster, M., Ghienne, J.F., Ruffet, G., and Rubino, J.L. (2019), Evolution of the northern Turkana Depression (East African Rift System, Kenya) during the Cenozoic rifting: New insights from the Ekitale Basin (28-25.5 Ma). Geological Journal. doi:10.1002/gj.3339

Renne, P.R., G. Balco, K.R. Ludwig, R. Mundil and K. Min (2011): Response to the comment by W.H. Schwarz et al. on "Joint determination of ^{40}K decay constants and ^{40}Ar*/^{40}K for the Fish Canyon sanidine standard, and improved accuracy for ^{40}Ar/^{39}Ar geochronology" by P.R. Renne et al. (2010). Geochimica et Cosmochimica Acta.

Rooney, T.O. (2010), Geochemical evidence of lithospheric thinning in the southern Main Ethiopian Rift: Lithos, v. 117, p. 33–48, https:// doi .org /10 .1016 /j.lithos .2010 .02 .002

Rooney, T.O. (2017), The Cenozoic magmatism of East-Africa: Part I. Flood basalts and pulsed magmatism. Lithos, 286-287, 264-301. doi: 10.1016/j.lithos.2017.05.014

Rosendahl, B.R. (1987), Architecture of continental rifts with special reference to East Africa. Annual Review of Earth and Planetary Sciences. doi:10.1146/annurev.earth.15.1.445

Saria, E., Calais, E., Altamimi, Z., Willis, P., and Farah, H. (2013), A new velocity field for Africa from combined GPS and DORIS space geodetic Solutions: Contribution to the definition of the African reference frame (AFREF). Journal of Geophysical Research: Solid Earth. doi:10.1002/jgrb.50137

Saria, E., Calais, E., Stamps, D.S., Delvaux, D., and Hartnady, C.J.H. (2014), Present-day kinematics of the East African Rift. Journal of Geophysical Research: Solid Earth. doi:10.1002/2013JB010901

Schouten, H., Klitgord, K.D., and Gallo, D.G. (1993), Edge-driven microplate kinematics. Journal of Geophysical Research: Solid Earth. doi:10.1029/92jb02749

Schaen, A.J., Jicha, B.R., Hodges, K.V., Vermeesch, Stelten, M.E., Mercer et al. (2020), Interpreting and reporting Ar-Ar geochronologic data. Geological Society of America Bulletin. doi:10.1130/B35560.1

Stamps, D.S., Calais, E., Saria, E., Hartnady, C., Nocquet, J.M., Ebinger, C.J., and Fernandes, R.M. (2008). A kinematic model for the East African Rift. Geophysical Research Letters. doi:10.1029/2007GL032781

Stamps, D.S., Saria, E., and Kreemer, C. (2018), A geodetic strain rate model for the East African Rift System. Scientific Reports. doi:10.1038/s41598-017-19097-w

Steiner, R.A., Rooney, T.O., Girard, G., Rogers, N., Ebinger, C.J., Peterson, L., and Phillips, R.K. (2021), Initial Cenozoic magmatic activity in East Africa: new geochemical constraints on magma distribution within the Eocene continental flood basalt province, in: Journal of the Geological Society . doi:10.1144/SP518-2020-262

Sullivan, G., Ebinger, C.J., Musila, M., Perry, M., , Kraus, E.R., Bastow, I., Bendick, B. (2024), Kinematics of rift linkage between the Eastern and Ethiopian rifts in the Turkana Depression, Africa. Basin Research, 36 (5). https://doi.org/10.1111/bre.12900

Tauxe, L. (2005), Inclination flattening and the geocentric axial dipole hypothesis. Earth and Planetary Science Letters. doi:10.1016/j.epsl.2005.01.027

Tauxe, L., Kent, D.V. (1982), A time framework based on magnetostratigraphy for the Siwalik sediments of the Khaur area, northern Pakistan. Paleogeography Palaeoclimatology. Paleoecology. doi:10.1016/0031-0182(82)90057-8.

Tauxe, L. (2005), Inclination flattening and the geocentric axial dipole hypothesisdoi:10.1016/j.epsl.2005.01.027

Uto, K., O. Ishizuka, A. Matsumoto, H. Kamioka and S. Togashi (1997): Laser-heating ^{40}Ar/^{39}Ar dating system of the Geological Survey of Japan: System outline and preliminary results. Bulletin of the Geological Survey of Japan, 48, 23-46

Vaes, B., Gallo, L.C., and van Hinsbergen, D.J. J. (2022), On Pole Position: Causes of dispersion of the paleomagnetic poles behind Apparent Polar Wander Paths. Journal of Geophysical Research, Solid Earth. doi: 10.1029/2022JB023953

Vaes, B., van Hinsbergen, D., & Paridaens, J. (2024), APWP-online.org: a Global Reference

Database and Open-Source Tools for Calculating Apparent Polar Wander Paths and Relative Paleomagnetic Displacements. тектопіка, 2(1), 174–189. doi:10.55575/tektonika2024.2.1.44

Versfelt, J., and Rosendahl, B.R. (1989), Relationships between pre-rift structure and rift architecture in Lakes Tanganyika and Malawi, East Africa. Nature (337), 354-357.

Wilke, F.D.H., P.J. O'Brien, A. Gerdes, M.J. Timmerman, M. Sudo and M.A. Khan (2010): The multistage exhumation history of the Kaghan Valley UHP series, NW Himalaya, Pakistan from U-Pb and ^{40}Ar/^{39}Ar ages. European Journal of Mineralogy, 22, 703-719

Woldegabriel, G., Aronson, J.L., and Walter, R.C. (1990), Geology, geochronology, and rift basin development in the central sector of the Main Ethiopia Rift. Bulletin of the Geological Society of America. doi:10.1130/0016-7606(1990)102<0439:GGARBD>2.3.CO;2

WoldeGabriel, G., Yemane, T., Suwa, G., White, T., and Asfaw, B. (1991), Age of volcanism and rifting in the Burji-Soyoma area, Amaro Horst, southern Main Ethiopian Rift: geo- and biochronologic data. Journal of African Earth Sciences. doi:10.1016/0899-5362(91)90107-A